Computational investigation of calcium aluminosilicate network dissolution

MASTER'S THESIS
CHEMICAL ENGINEERING
AALBORG UNIVERSITY
JUNE 1ST 2022
ANDERS MOSE SCHADE

AALBORG UNIVERSITY
STUDENT REPORT

Department of Chemistry and Bioscience
Chemical Engineering
Fredrik Bajers Vej 7H
9220 Aalborg East
`http://www.bio.aau.dk`

Title:

Computational investigation of calcium aluminosilicate network dissolution

Project:

Master's Thesis

Project period:

September 2022 - June 2023

Student:

Anders Mose Schade – 20182487

Advisors:

Morten M. Smedskjær

Tiffany R. Walsh
Deakin University

Martin P. Andersson
Technical University of Denmark

Number of pages: 49
Appendices: 4
Finished: 01-06-2022

Abstract:

The dissolution property of stone wool fibres is essential for product stability and health safety. The stone wool material is amorphous with a large network of network formers (NF) and network modifiers placed within the network. The primary constituents of stone wool are SiO_2, Al_2O_3 and CaO, and calcium aluminosilicate is thus used as a model system to reduce the complexity. The amorphous network breaks by a hydrolysis reaction creating two hydroxyl groups in place of the bridging oxygen. The underlying mechanism responsible for this property is not entirely understood.
Therefore, the computational methods of Molecular Dynamics (MD) and Density Functional Theory (DFT) are employed to enlighten this reaction. Using the novel *wet-GS* force field in MD, stationary H_2O molecules are found which are stabilised by hydrogen bonding. These are used for reaction pathway analysis of the hydrolysis reaction of NFs in DFT using a small sphere of aluminosilicate glass to determine activation energies (Ea) for the hydrolysis of NF bonds. The Al-Al linkage is most likely to break with an Ea of 47 to 85 kJ/mol, while Si-Si and Si-Al are equally likely to break with Eas in the 85 to 165 kJ/mol range. No significant difference in Ea for Qn groups is observed. Including a second H_2O in the reaction pathway analysis did not reduce the Eas because the reaction mechanism remained the same.

Preface

This study is a part of the WOODI (wool dissolution) project started by ROCKWOOL International A/S in collaboration with Technical University of Denmark, Deakin University in Melbourne, Australia and Curtin University in Perth, Australia. During the fall of 2022, I visited the computational chemistry group at the Institute for Frontier Materials at Deakin University to work together with the WOODI members based in Australia. While in Australia, I also presented the progress of the WOODI project at the Advanced Materials and Sustainable Technologies 2022 conference in Cairns, Australia. The work presented herein is a continuation of research by former and current members of the WOODI project. The current project uses both published and unpublished work from the WOODI project, and references will be made (whether published or unpublished). The raw data, scripts for data processing, production of all the plots and statistical tests are provided in the supplementary material handed in along with the Master's thesis.

Thanks to Professor Tiffany Walsh and Professor Martin Andersson for supervision throughout the project. Thanks to Chief Engineer at ROCKWOOL International A/S, Mette Solvang, and the WOODI group for the opportunity to participate in the project. A special thanks to Professor Tiffany Walsh and her research group at Deakin University for their hospitality during my visit to Australia. Thanks to Professor Morten M. Smedskjær for the final remarks. Lastly, thanks to ROCKWOOL International A/S, Danish Data Science Academy and Deakin University for partially funding my travels to Australia and attendance at the Advanced Materials and Sustainable Technologies 2022 conference.

Danish Summary

Opløseligheden af stenuldsfibre er vigtig en parameter for stenuldsprodukters stabilitet og sundhedsfare. Stenuld er et amorft materiale med et stort, sammenhængende netværk af network formers (NFs) og network modifiers (NMs), der er placeret i netværket. De primære bestanddele i stenuldglas er SiO_2, Al_2O_3 og CaO, og derfor vil calcium aluminosilicate (CAS) glas blive benyttet som et modelsystem for stenuldglas, som udover de primære bestanddele består af en række andre NMs. Stenuldets netværk kan blive brudt af hydrolysereaktioner ved, at et vandmolekyle bryder en netværksbinding og skaber to hydroxylgrupper. De grundlæggende mekanismer for denne reaktion er ikke helt forstået.

Derfor vil kemiske simulerings- og beregningsmetoder, Molecular Dynamics (MD) og Density Functional Theory (DFT), blive brugt til at undersøge denne reaktion. Ved hjælp af det nyudviklede *wet-GS* kraftfelt i MD, bliver stationære vandmolekyler fundet, og de bliver stabiliseret af intermolekylære hydrogen bindinger til hydroxylgrupper på overfladen af CAS glasset. De stationære vandmolekyler bliver implicit brugt i DFT udregninger til at placere vandmolekyler, således at de hydrogenbinder til tilsvarende hydroxylgrupper i et mindre aluminosilicate glas system. Her bliver aktiveringsenergien af tre bindingstyper undersøgt: Si-Si, Si-Al og Al-Al (alle med et oxygen atom imellem). Disse er inddelt afhængigt af, hvor mange netværksbindinger hver NF har (Q3, Q2 eller Q1).

Det bliver konkluderet, at Al-Al bindingen har den laveste aktiveringsenergi mellem 47 og 85 kJ/mol og er derfor mest tilbøjelig til at blive hydrolyseret. Si-Si og Si-Al har tilsvarende tilbøjelighed til at blive hydrolyseret med en aktiveringsenergi mellem 85 kJ/mol og 165 kJ/mol. Der bliver ikke observeret nogen signifikant forskel mellem Qn grupper inden for hver bindingstype. Indflydelsen af et ekstra vandmolekyle er også undersøgt, hvor der ikke bliver observeret nogen signifikant påvirkning af dataene. Dette bliver tilskrevet, at reaktionsmekanismen forbliver den samme ved inklusionen af ekstra vandmolekyle.

List of abbreviations

Abbreviations used throughout this project are listed here in alphabetical order.

Abbreviation		**Description**
BO	–	bridging oxygen
CAS	–	calcium aluminosilicate
COSMO	–	Conductor-like Solvation Model
DFT	–	Density Functional Theory
GGA	–	generalised gradient approximation
GS	–	Guillot-Sator (potential)
hyper-GGA	–	hyper-generalised gradient approximation
LAMMPS	–	Large-scale Atomic/Molecular Massively Parallel Simulator
LDA	–	local density approximation
MARI-J	–	multiple accelerated resolution of identity
MD	–	Molecular Dynamics
meta-GGA	–	meta-generalised gradient approximation
N	–	number of atoms
NBO	–	non-bridging oxygen
NCI	–	National Computing Infrastructure
NF	–	network former
NPT	–	isothermal-isobaric ensemble
NVT	–	canonical ensemble
PMF	–	potential of mean force
Qn	–	n number of network forming bonds for network former
RDF	–	radial distribution function
RI	–	resolution of identity
SAS	–	solvent accessible surface
SCF	–	self-consistent field
SES	–	solvent excluded surface
SHIK	–	Sundarararaman, Huang, Ispas, Kob (potential)
T_f	–	fictive temperature
T_m	–	melting temperature
TOF-SIMS	–	time-of-flight secondary ion mass-spectroscopy
TZVP	–	triple-zeta valence polarization
WOODI	–	Wool dissolution project
wet-GS	–	extension of the Guillot-Sator potential with H_2O parameters
XPS	–	X-ray Photoelectron spectroscopy

Contents

Introduction

1

Stone wool glass fibre is widely used as thermal insulation in the construction industry to reduce the energy needed to regulate the temperature of buildings due to its low thermal conductivity. [Yue and Solvang, 2021] Stone wool glass fibre also has excellent flame retardant properties because of the high-temperature stability of the fibres, which also contributes to its wide use. [Moesgaard et al., 2007; Smedskjær et al., 2010] Production of the insulating material involves melting basalt and diabase stone material which is hyperquenched, spun into a fibrous material and sprayed with a binder to give the material sufficient mechanical and hydrophobic properties. Other crude materials, such as waste products from other industries, can also be used in the production. [Guldberg et al., 2000; Yue and Solvang, 2021] Stone wool glass fibre is thus an amorphous material primarily consisting of SiO_2, Al_2O_3 and CaO with lesser amounts of MgO, Fe_2O_3, TiO_2, Na_2O and K_2O. The amorphous state of the stone wool glass means that it is comprised of an extensive network of so-called network formers (NFs), such as Si and Al, with O atoms in between. The other constituents of the glass are called network modifiers (NMs), and they are present in vacancies in the glass where they charge balance the network. [Guldberg et al., 2000; Wohlleben et al., 2017]

In 2002, the International Agency for Research on Cancer declassified stone wool as carcinogenic after being classified as such in 1988 by the same organisation. The suspicion of carcinogenicity emerged due to similarities in the structure of stone wool fibres and the highly carcinogenic asbestos fibres, in addition to data suggesting a relationship between exposure to stone wool fibres and lung cancer. [IARC, 2002] The declassification occurred due to the development of more soluble stone wool compositions and extensive research in the insulation industry demonstrating the material's biosolubility (ability to get dissolved in biological systems) after inhalation. [Guldberg et al., 2000; IARC, 2002] However, the beneficial biosolubility also has drawbacks in that exposure to humidity can affect the durability of the stone wool by reaction of ambient moisture with stone wool fibres. [Vrána, 2007; Ivanič et al., 2020] The material must be balanced between being readily biosoluble and sufficiently stable in humid conditions to avoid performance loss after installation. The dissolution rate is, therefore, an essential parameter for insulating materials, but the underlying mechanism responsible for the dissolution of the amorphous materials has not yet been uncovered. The dissolution of stone wool glass has been studied experimentally where several responsible processes are suggested [Petit et al., 1990; Campopiano et al., 2014; Wohlleben et al., 2017; Barly et al., 2019; Okhrimenko et al., 2020; 2022; Guldberg et al., 2000]. Among the proposed reaction mechanisms are hydrolysis of the NFs and ion exchange of the NMs, which leads to relative enrichment of the NF content in the surface layer [Petit et al., 1990; Barly et al., 2019; Okhrimenko et al., 2022]. It is observed that increasing Al_2O_3 content also increases the dissolution rate of the stone wool glass [Guldberg et al., 2000]. pH is found to greatly influence the dissolution rate and reaction mechanism [Okhrimenko et al., 2020]. Therefore all of the experimental studies need to take pH into account. Okhrimenko et al. [2022] partly investigated surface hydroxyls on the fibres and ascribed them great influence on the reactivity of the stone wool glass in aqueous solutions.

To further shed light on the mechanism responsible for dissolving the stone wool glass, computational methods will be utilised to investigate the hydrolysis of the NFs. The advantage of a computational approach is that the underlying reaction mechanisms responsible for what is experimentally observed can be explored on an atomic level. Energies associated with breaking and forming bonds in the system can be quantified and compared to evaluate how the reactions occur.

Problem statement

2

The present study will investigate the dissolution mechanism of NFs in amorphous calcium aluminosilicate (CAS) glass as a model system for stone wool glass. To limit the complexity of the stone wool glass system, many of the NMs are excluded while keeping the primary constituents of the material. The simplification of the system is considered a valid starting point for investigating the stone wool glass [Turchi et al., 2021].

The dissolution of the CAS glass network will be investigated using Molecular Dynamics (MD) simulations and Density Functional Theory (DFT) calculations. The MD simulations can be used to simulate relatively large systems (multiple thousand atoms), which is sufficient to simulate the interface between the CAS glass and water. From these simulations, the structural features of this interface can be extracted. The novel *wet-GS* potential developed in the WOODI project will be used to simulate the CAS to water interface. On the other hand, DFT cannot be used on large systems without great computational expense, as these calculations are based on the electronic configuration of the atoms. Instead, DFT can be utilised to accurately investigate the reaction mechanism in a smaller system. Using the structural features identified via MD simulations, DFT will be used to calculate the activation energies associated with breaking the network forming bonds by hydrolysis reactions. The study will therefore aim to answer the following problem statement:

What is the reaction pathway for the dissolution of network formers in calcium aluminosilicate glass?

Theory 3

3.1 The chemistry of stone wool glass

Stone wool is an amorphous material meaning that its structure possesses no long-range order at the atomic level [Yue and Solvang, 2021]. Instead, it is highly unordered and is essentially locked into a liquid-like structure in solid form. The amorphous state of matter can be achieved in several ways, but for stone wool glass, it is achieved by a melt-quench process, which involves rapidly cooling a melt of molten stone. The cooling should be sufficiently fast to ensure that the melt does not undergo crystallisation by arranging into crystalline structures when transitioning from liquid to solid. This results in an undercooled frozen-in liquid, and in other words: a solid with the structure of a liquid. [Shelby, 2005; Conrady, 2019] The transition to the amorphous state can be understood using Figure 3.1.

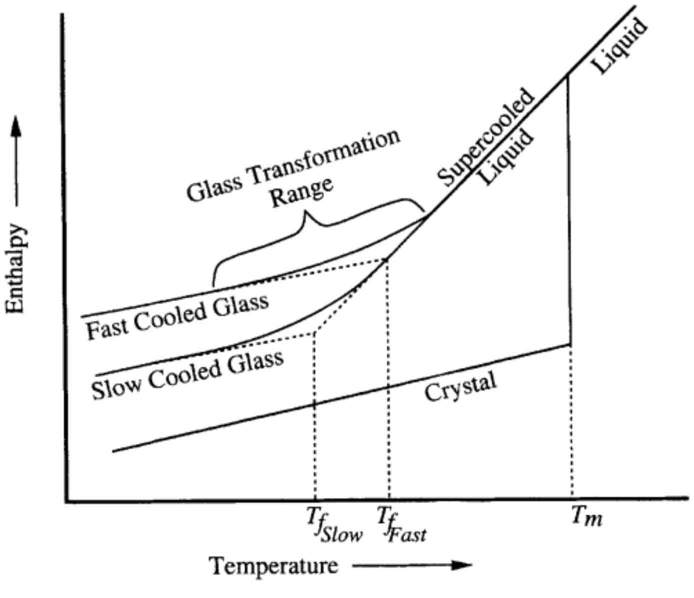

Figure 3.1. Theoretical plot of glass formation with enthalpy as a function of temperature. T_m is the melting temperature. $T_{f_{slow}}$ is the fictive temperature when the cooling rate is slow, and $T_{f_{fast}}$ is the fictive temperature when the cooling rate is fast. [Shelby, 2005]

When a crystal is heated beyond its melting temperature (T_m), it transitions to the higher enthalpy state of a liquid. When it is cooled below T_m, it regains the crystalline state under normal circumstances. However, if the liquid is cooled sufficiently fast, the large drop in enthalpy does not occur, and it instead has a smooth decrease in enthalpy and becomes a supercooled (or undercooled) liquid before finally transitioning to the amorphous state. The glassy material then exhibits a *fictive temperature* (T_f), meaning that glass has a structure similar to the equilibrium liquid at T_f. This is also the point where the glass leaves thermodynamic equilibrium. Figure 3.1 also shows that the higher the cooling rate, the higher the T_f. [Shelby, 2005; Conrady, 2019]

Stone wool falls within the category of oxide glasses, which consists of large networks with NFs covalently bonded to O atoms in an alternating manner. The NFs are typically atoms with a tendency to form tetrahedral units, such as Si, B or Al. Within the field of amorphous materials, there is a *Qn* notation to denote how many bridging Os (BOs) each NF is bonded to. If it is bonded to four BOs, it is a *Q4* and so on. The amorphous system also contains ions that charge stabilise non-bridging oxygens (NBOs) in the network. The NBOs are defects in the amorphous network that occur when O only binds to one (instead of two) NFs. Therefore, the O has a negative charge which is stabilised by the positively charged NMs. These are typically monovalent or divalent ions such as Na, K, Ca or Mg. Many methods can be used to determine which role a given oxide will adopt in a glass based on different parameters. One of the more widely used definitions is Dietzel's field strength approach

$$FS = \frac{Z}{(r_c + r_o)^2}, \tag{3.1}$$

where Z is the ionic charge of the cation and r_c and r_o are the radii of the cation and oxygen, respectively. Atoms with high field strength ($FS > 1\text{Å}^{-2}$) are NFs, atoms with low field strength ($FS < 0.35\text{Å}^{-2}$) are NMs. If the value lies between these two limits, it is categorised as an intermediate and assumes either the role of an NF or an NM. This definition suggests that both a small size and a high charge of a cation favour the formation of amorphous oxides. [Bourhis, 2014]

The glass system to be investigated in this study is illustrated in Figure 3.2.

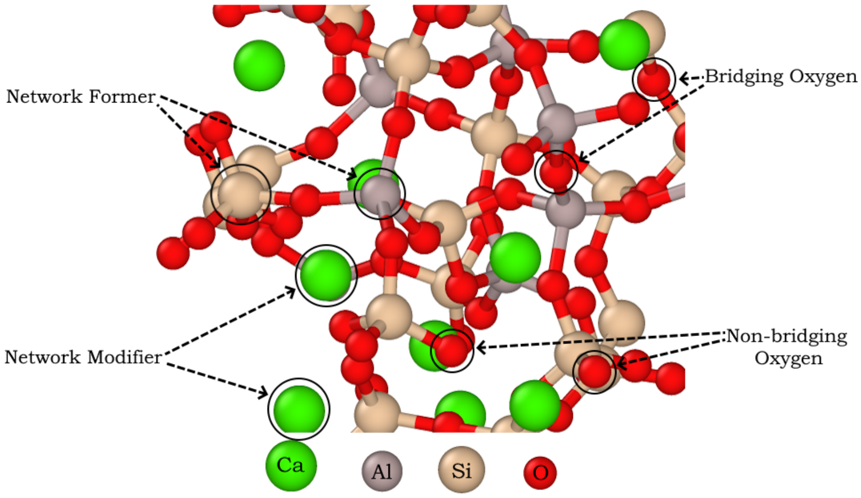

Figure 3.2. Small cutout of the CAS glass system investigated in this study. The radii of the atoms are scaled to 1/4 of their actual size (van der Waals radius). Green atoms are Ca, grey atoms are Al, brown atoms are Si and red atoms are O. Visualised using the Ovito software [Stukowski, 2010].

Figure 3.2 illustrates how the glassy network of CAS consists of the two types of NFs, Si and Al, and an O atom separates each NF. Three types of network linkages are present in the network: Si-O-Si, Si-O-Al or Al-O-Al. The NM in this system is Ca. These are not bonded covalently in the network but are present throughout the network to compensate for negatively charged species. If an O does not link to two NFs and instead only one, it needs to be charge stabilised by the presence of Ca. Additionally, when Al forms tetrahedral units, it needs to be charge stabilised by the network modifiers due to its native charge of +3.

3.1.1 Production of stone wool glass

Stone wool glass is made from natural minerals, such as basalt, olivine and dolomite, which are melted by a cupola or electric- or gas-heated furnace into a homogeneous mixture. The melt is then poured into a spinning chamber where one to four spinning wheels hyper-quench and draw the material into the characteristic fibres that make up the stone wool material. The spinning wheels are known as *cascade spinners* and can be seen in Figure 3.3.

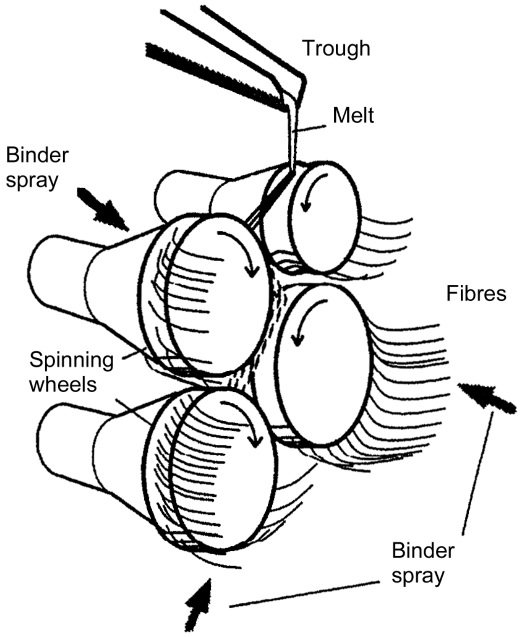

Figure 3.3. Illustration of the spinning chamber where stone wool fibres are formed. The melt is poured into the chamber via a trough onto the cascade spinners. The stone wool is spun into fibres, and sprayed with a binder. Typically, air jets assist in releasing the fibres from the wheels. [Thermal Insulation Manufacturers Association, 1993]

In the spinning chamber, the liquid transitions from a melt with low viscosity to an amorphous solid. Air jets in the chamber assist in cooling and releasing the fibres from the wheels. Meanwhile, the fibres are also sprayed with a binder solution that is important for the mechanical properties of the final material. The fibres are collected and transferred to a curing oven where polymerisation of the binder occurs. Finally, the cured stone wool is cut into regular shapes and packed for use in the construction industry. [Yue and Solvang, 2021]

The typical composition range of stone wool glass is listed in 3.1 along with the typical composition converted into molar percentages. The primary constituents are SiO_2, Al_2O_3, and CaO with other network modifiers in lower amounts as well.

Table 3.1. Typical chemical composition range of a stone wool glass.[Yue and Solvang, 2021] mol % are based on the mean wt% of the ranges. The molar mass for $Na_2O + K_2O$ is a mean of the two oxides.

Oxides	[wt%]	[mol%]
SiO_2	36 − 42%	41%
Al_2O_3	17 − 24%	13%
CaO	14 − 25 %	22%
MgO	2 − 12 %	11%
FeO	4 − 11%	7 %
TiO_2	0.5 − 3%	1 %
$Na_2O + K_2O$	0 − 12%	5 %

In contrast to glass wool, which is also an insulation material, stone wool has a higher content of divalent modifier ions. This gives the stone wool glass a higher melting point than glass wool. [Yue and Solvang, 2021] The presence of FeO and MgO also gives stone wool its high-temperature stability by forming a nanocrystalline layer when heated to 1000 °C [Smedskjær et al., 2010].

3.1.2 Dissolution of the stone wool system

A CAS glass has a network consisting of Si and Al with Ca acting as the network modifier. The network bonds can be broken via hydrolysis reactions. Here, NF is either Si or Al

$$\mathrm{NF{-}O{-}NF} + \mathrm{H_2O} \longrightarrow 2\,\mathrm{NF{-}OH}. \tag{3.2}$$

This reaction leads to depolymerisation of the glass network and leaves behind two hydroxyl (OH) groups. [Baral et al., 2020; Kagan et al., 2014] This reaction primarily occurs on the surface of the glass as it requires BOs that are accessible by H_2O. As such, the surface of the CAS glass can be expected to be covered with hydroxyl groups when exposed to water. [Baral et al., 2020; Morrow et al., 2009; Vuković et al., 2023] In recent years, the hydrolysis of network forming bonds in aluminosilicate glass and the dissolution of stone wool glass has become a field of scientific interest [Okhrimenko et al., 2020; 2022; Turchi et al., 2021; Baral et al., 2020; Zhang et al., 2022].

Previous DFT studies of hydrolysis of Al/Si-O-Al/Si (excluding Al-O-Al) found that the bonds involving Al have a lower energy barrier than those without. These studies only investigated simplified systems involving two completely hydroxylated network forming species that are not bonded to an amorphous network. It was also concluded that the protonation state of the species involved in the hydrolysis affects the energy barrier. [Morrow et al., 2009; Nangia and Garrison, 2008; Xiao and Lasaga, 1994] Some studies show that in alkali aluminosilicate glasses, the hydrolysis does not occur by depolymerisation of the network and instead forms Si-OH-Al and releases free monovalent network modifier bonded to OH (M-OH), which could be expected to occur in CAS glass. However, this mechanism is disputed by other studies, which instead support the depolymerisation mechanism. [Baral et al., 2020] The argument here illustrates how the underlying reaction mechanism responsible for the hydrolysis is debated.

Zhang et al. [2022] found that the activation energy of small $Al(OH)_3{-}O{-}Si(OH)_3$ and $Si(OH)_3{-}O{-}Si(OH)_3$ clusters can be reduced by the introduction of an additional H_2O in the hydrolysis through H^+ exchange between the two H_2O molecules. An MD simulation study using the diffuse charge reactive pair potential and potential mean of force (PMF) calculations, Damodaran et al. [2022], found the activation barriers for hydrolysis of NF-O-NF involving Al had an activation barrier half of those without.

The hydrolysis of the Al-O-Al linkage is less studied than the Si-O-Si/Al linkage due to the inclination of zeolites (an aluminosilicate mineral) to follow Löwenstein's rule, which forbids tetrahedral units of alumina to be placed adjacent to each other and therefore Al-O-Al linkages cannot exist. However, numerous examples of experimental violations of this rule exist in the literature, and computational studies often disregard this rule to reduce the computational expense in the calculations of these systems. [Fletcher et al., 2017] It has also been experimentally demonstrated that aluminosilicate glasses greatly violate Löwenstein's rule and an increasing proportion of Al-O-Al linkages are found with increasing field strength of the modifier ions in the amorphous system (inclusion of Na, Li and Ca was studied). [Lee and Stebbins, 2000] Löwenstein's rule is therefore disregarded in this project, and Al-O-Al linkages are investigated on par with the other types of network forming linkages in the glass.

Amorphous SiO_2 systems have been studied more extensively. Kagan et al. [2014] investigated the dissolution of amorphous SiO_2 starting from Q4 and stepwisely hydrolysed to Q0 (free $Si(OH)_4$) with one neutral H_2O using MD and the PMF method. The reactions of the Q3 to Q2 species were found to have the highest activation energy and were deemed to be the rate limiting step in the complete dissolution. The authors also investigated the hydrolysis reaction mechanism and found that the activation energy depends on the orientation at which the H_2O attacks the network linkage. The magnitude of the activation energies for the different Qn species was attributed to the amount of strain associated with forming the pentacoordinated transition state, such that species with fewer network bonds have lower activation energies. It should be noted that in their paper, the differences between the Qn groups are small and all groups have large standard deviations. Walsh et al. [2000] suggested that the inclusion of multiple H_2Os in the hydrolysis of amorphous SiO_2 can reduce the activation energy by facilitating different reaction mechanisms.

Even though many studies that investigate the hydrolysis of aluminosilicate (and similar systems) exist, no DFT (or any other first-principles technique) study has investigated the complete hydrolysis ($Q_3 \longrightarrow Q_0$) in a larger system. The complete hydrolysis is interesting due to the possibility of specific hydrolysis reactions being rate limiting. Therefore, the focus of this study is drawn to this aspect of the hydrolysis.

3.2 Molecular Dynamics simulations

Molecular Dynamics (MD) is a widely used simulation technique for chemical systems. MD treat atoms as classical mechanical objects floating in a void. The atoms have forces acting on each other, creating attraction and repulsion to other atoms, replicating the effect of electrons. The motion of the atoms in the simulation is calculated using classical mechanics and Newton's laws of motion. Especially, Newton's second law of motion is useful in calculating the forces of atoms acting on each other

$$f_i = m_i \cdot \frac{\partial^2 r_i}{\partial t^2}, \tag{3.3}$$

where f_i is the force on atom i, m_i is the mass of atom i, r_i is the position of atom i, and t is time. [Leach, 2001]

MD simulations typically consist of many thousands of atoms and millions of time steps. Every time step, the forces between atoms must be calculated, which is nearly impossible to do analytically. Instead, finite difference methods are used to numerically solve the many-body problem of calculating the forces between atoms. Common for many finite difference methods are that they are based on Taylor series expansions to calculate the positions, velocities and accelerations of the atoms in the system. A commonly used algorithm for calculating new positions ($r(t + \Delta t)$) is the Verlet algorithm which uses the positions of the atoms at the previous timestep ($r(t - \Delta t)$) and the positions ($r(t)$) and accelerations ($a(t)$) at the current timestep,

$$r(t + \Delta t) = 2r(t) - r(t - \Delta t) + a(t)\Delta t^2. \tag{3.4}$$

The Verlet algorithm is a fast and efficient way to calculate the new positions of the atoms in the system. Because velocity is not explicitly included in the calculation, a variation of the Verlet algorithm has been developed called the Velocity Verlet algorithm, which calculates positions, velocity and acceleration simultaneously and is the most widely used algorithm for these calculations in MD. [Leach, 2001; Du, 2019]

3.2.1 Force fields

In MD simulations, the force between atoms is calculated using force fields (or potentials). The description of the interactions between the atoms (in this case, the force field) is a critical input in the MD simulations as it dictates the interatomic interactions in the system. The function for a potential in a system with N atoms is

$$U(r_N) = \sum_{i}^{N} U_1(r_i) + \sum_{i}^{N} \sum_{j>i}^{N} U_2(r_i, r_j) + \sum_{i}^{N} \sum_{j>i}^{N} \sum_{k>j}^{N} U_3(r_i, r_j, r_k) + \dots , \tag{3.5}$$

where $U(r_N)$ is the total potential energy in the system, the first term (U_1) is the one-body interaction due to an external field, the second term (U_2) is two-body interactions due to pair interactions, and the third term (U_3) is three-body interactions, e.g. used to constrain bond angles. Usually, two-body interactions are used to calculate the force between atoms in ionocovalent solids, such as oxide glass systems. This means that the force field can be reduced to include long-range attractive forces and short-range repulsive forces. The long-range forces are typically a Coulumbic term. The dispersion term has both long- and short-range contributions. These two terms are expressed in simple form as

$$U(r_N) = \sum_{i}^{N} \sum_{j>i}^{N} \Big(\frac{q_i q_j}{4\pi r_{ij} \varepsilon_0} + \frac{A}{r_{ij}} \Big). \tag{3.6}$$

One of the most commonly used potentials for amorphous systems is the Buckingham potential, which has the form

$$U(r_{ij}) = A_{ij} \cdot \mathrm{e}^{-r_{ij}/B_{ij}} - \frac{C_{ij}}{r_{ij}^6}, \tag{3.7}$$

where A_{ij}, B_{ij} and C_{ij} are parameters for the specific atom pair *ij*. The Buckingham potential is composed of terms from the Lennard-Jones and Morse potentials, where the first term is a repulsive term from the Morse potential and the second term is van der Waals attraction from the Lennard-Jones potential. [Du, 2019; Leach, 2001] Because potentials are fitted to empirical data from experiments and/or first-principles calculations, novel force fields can have many different forms, parameters, and terms. The advantage of MD simulations is that they are run by relatively simple formulas enabling the simulation of large systems. The force fields can, however, have a limited application field where it only works well with the systems from which its parameters were fitted to. This can be validated by comparing data of physical properties from simulations to data from experiments and first-principles calculations. [Guillot and Sator, 2007; Sundararaman et al., 2018]

For the simulation of CAS systems, numerous potentials can be used. The elements in the CAS system are very common in nature, and most force fields that can be used for glasses also have parameters for these elements. A previous study by the WOODI group [Turchi et al., 2021] investigated both the GS and Sundararaman, Huang, Ispas, Kob (SHIK) potential to simulate CAS glass as a model system for stone wool glass. Both potentials could adequately simulate the bulk CAS glass properties, including the proportion of linkage types and defect concentrations. The ultimate goal for the WOODI project is to simulate real stone wool which, besides the elements in CAS, are Na, K, Mg, Fe and Ti. Keeping the scope of the overall project in mind, it is important to use a force field with parameters for all these elements. Further deciding on which force field to use can then depend on their accuracy and efficiency. As force fields are mathematical approximations of atomic interactions for specific systems, there typically is a trade-off between accurate imitation of the chemical systems and computational efficiency.

The GS potential has been developed to model basaltic melts efficiently. The potential already includes parameters for all the relevant elements for simulation of stone wool glass. It does not, however, have parameters for the interaction between CAS glass and liquid H_2O. Therefore, the GS potential has been extended to also have parameters for H_2O and hydroxyl groups on the CAS surface. The extended GS potential will be denoted *wet-GS* which is further described in Section 4.1.1 and the parameters for the potential are seen in Appendix A.

3.3 Density Functional Theory

Density Functional Theory (DFT) is a quantum mechanical technique that can approximate solutions to the Schrödinger equation to determine the electronic structure of atoms, molecules and condensed matter. DFT can be used to obtain highly accurate descriptions of chemical systems and transition states based on the electrons in the system. In this study, the method will be used to investigate the hydrolysis reaction of the network forming bonds in the CAS glass.

DFT is based on the Born-Oppenheimer approximation which states that the electronic and nuclear motions can be treated separately due to the inconsiderable mass of the electrons compared to nuclei. The electrons can rapidly adjust to the motion of their nucleus and therefore the energy of molecules in electronic ground states can be obtained as a function of the nuclei coordinates. [Sholl and Steckel, 2009; Leach, 2001]

The simplest form of the time-independent Schrödinger equation is

$$H\psi = \psi E, \tag{3.8}$$

where H is the Hamiltonian operator (operator for the total energy of a system), ψ is an electronic wave function and the eigenstates for the Hamiltonian operator, and E is and ground-state energy of the electrons and the eigenvalue. This means that when the Hamilton operator, H, acts on the wave function, ψ, the same wave function times the ground-state energy, E, is returned. The full time-independent Schrödinger equation is

$$\left[\frac{\hbar^2}{2m}\sum_i^N \nabla_i^2 + \sum_i^N V(\mathbf{r}_i) + \sum_i^N \sum_{j<i} U(\mathbf{r}_i, \mathbf{r}_j)\right]\psi = E\psi, \tag{3.9}$$

where m is the mass of the electron and $\hbar$ is the reduced Planck's (or Dirac) constant. The first term in Equation (3.9) describes the kinetic energy of each electron, the second term describes the interaction energy between each electron and the nuclei, and the third term describes the interaction energy between all the different electrons. ψ is the wave function for the position of all N electrons, $\psi = \psi(\mathbf{r}_1, ..., \mathbf{r}_N)$, which can be approximated as the Slater determinant, $\psi = \psi_1(\mathbf{r})\psi_2(\mathbf{r}), ..., \psi_N(\mathbf{r})$, comprising entries made from individual electron wave functions (which ultimately are deemed atomic/molecular orbitals). [Sholl and Steckel, 2009; Leach, 2001]

Even though the Schrödinger equation is the fundamental problem of quantum mechanics, the wave function for a collection of coordinates cannot be observed or measured. However, the probability that electrons are at certain positions can be measured. The density of electrons at a specific spatial position can be expressed as

$$n(\mathbf{r}) = 2\sum_i^N \psi_i^*(\mathbf{r})\psi_i(\mathbf{r}) \tag{3.10}$$

where ψ^* is the complex conjugate to ψ. The factor of 2 is present due to the Pauli exclusion principle, which states that two electrons can only occupy the same spatial electronic wave function if they have different spins. [Sholl and Steckel, 2009]

The foundation of DFT is built on two theorems by Hohenberg and Kohn:

1. *The ground-state energy from Schrödinger's equation is a unique functional of the electron density*
2. *The electron density that minimises the energy of the overall functional is the true electron density corresponding to the full solution of the Schrödinger equation.*

The first theorem states that there is a direct correlation between the ground-state wave function and the ground-state electron density. This means there exists a functional that expresses the ground-state energy in terms of the electron density, $E[n(\mathbf{r})]$. Consequently, the Schrödinger equation can be solved by a function of electron density, which is a function of three dimensions, instead of the wave function, which is a function of $3N$ dimensions (where N is the number of electrons). The second theorem states that the solution to the full Schrödinger equation is an electron density that minimises the total energy of the functional, which means that the true electron density can be determined iteratively by finding a minimum. [Sholl and Steckel, 2009; Leach, 2001] The functional described by the theorems can be expressed in terms of single-electron wave functions, $\psi_i(\mathbf{r})$,

$$E[\{\psi_i\}] = \frac{\hbar^2}{m}\sum_i \int \psi_i^* \nabla^2 \psi_i d^3r + \int V(\mathbf{r})n(\mathbf{r})d^3r \tag{3.11}$$

$$+ \frac{e^2}{2}\int\int \frac{n(\mathbf{r})n(\mathbf{r}')}{|\mathbf{r}-\mathbf{r}'|}d^3r d^3r' + E_{ion} + E_{XC}[\{\psi_i\}] \tag{3.12}$$

where the first four terms are the known contributions, which in order of appearance are: electron kinetic energies, Coulombic interactions between nuclei and electrons, Coulombic interaction between pairs of electrons and finally, the Coulombic interactions between pairs of nuclei. The fifth term is the exchange-correlation functional which covers all of the effects that are not included in the known terms. [Sholl and Steckel, 2009]

Kohn and Sham showed that determining the right electron density can be done by solving equations that only involve a single electron, rather than all electrons as Equation (3.9) requires,

$$\left[-\frac{\hbar^2}{2m}\nabla^2 + V(\mathbf{r}) + V_H(\mathbf{r}) + V_{XC}(\mathbf{r})\right]\psi_i(\mathbf{r}) = \varepsilon_i\psi_i(\mathbf{r}). \tag{3.13}$$

V is the potential for the interaction between electron and atomic nuclei, V_H is the Hartree potential and V_{XC} is the exchange-correlation potential. The Hartree potential is

$$V_H(\mathbf{r}) = e^2 \int \frac{n(\mathbf{r}')}{|\mathbf{r}-\mathbf{r}'|} d^3r'. \tag{3.14}$$

This potential describes the Coulumbic repulsion between the electron considered in Equation (3.13) and the electron density of all the electrons in the system. In this, a self-interaction contribution is also included as the investigated electron is also a part of the total electron density. This is an unphysical interaction and the correction of this is one of many contributions included in V_{XC}. Equation (3.13) looks similar to Equation (3.9), but without the summation signs because Equation (3.13) is for single-electron wave functions. [Sholl and Steckel, 2009]

Solving the Kohn-Sham equation (Equation (3.13)) requires an iterative method because the Kohn-Sham equation involves the Hartree potential, which includes the electron density. But the electron density is determined by the single-electron wave functions and those are obtained by solving the Kohn-Sham equation. Therefore, an algorithm is applied to obtain a self-consistent result including an initial electron density, which is successively updated to a trial electron density until the final electron density is obtained by a result converging the resultant density within a given threshold. The algorithm for obtaining converging results within a set threshold is known as the self-consistent field (SCF) method and is commonly used in Kohn-Sham DFT calculations. [Sholl and Steckel, 2009; Leach, 2001]

3.3.1 Exchange-correlation functionals

When performing DFT calculations, an important decision is which exchange-correlation functional to use, somewhat analogous to the force fields in MD simulations. The search for exchange-correlation functionals that can yield accurate approximations of the total energy has previously been a limitation in the wide use of DFT. The development of new functionals that are able to yield more accurate approximations has established DFT as a reliable tool for calculating the electronic structure of atoms and molecules. [Jones, 2015]

The exchange-correlation functionals are important in obtaining favourable and precise results. As with the force fields in MD simulations, the functionals are usually based on empirical or first-principles data to which the functional can be fitted. They can provide very accurate results for certain problems, especially problems closely related to the system of the training set. However, some DFT functionals are nonempirical and have been constructed to make use of the known constraints on the Kohn-Sham functional by satisfying a few selected theoretical constraints that DFT calculation should respect. The accuracy of nonempirical functionals can be improved by including more constraints, but the objective of the exchange-correlation functional is to cover all of the interactions that are not known. It is therefore not easy to include more constraints in the functional. [Sholl and Steckel, 2009]

The exchange-correlation functionals can be divided into groups depending on how much physical information they include and by extension how accurate they should be. The simplest group of functionals is the local density approximation (LDA) where it is assumed that the electron gas is uniform in space and is the same as the local electron density. The next group is the generalised gradient approximation (GGA) which assumes that the electron densities are not uniform by including spatial variation in the electron density. The inclusion of spatial variation should make GGA functionals more accurate than LDA. The third group is called meta-GGA and this is where the most common functionals with a localised basis set are placed. These functionals include the second derivative of the electron density and dependence on the kinetic energy of the orbitals. The final functional group includes contributions from the exact exchange energy and are called hyper-GGAs (or hybrid functionals). They build on the meta-GGA functionals and include nonempirical fitting. It should be noted that even though the functionals in higher groups of complexity include more physical information, they are not always more accurate. In particular, the empirical nature of many functionals limits their accuracy to systems similar to those used to develop the functional. In general, GGA functionals are the most widely used, and in many situations these provide adequately accurate results without too much computational expense. [Sholl and Steckel, 2009]

3.3.2 Implicit solvation models

Investigating the breakage of network forming bonds by hydrolysis requires that the solvation effects are considered to ensure that the energy associated with breaking the bonds is accurate. When solvation effects are investigated by explicit means, a large number of solvent molecules have to be included in the simulations or calculations to capture the equilibrium state of the solvation. This is unfeasible using computationally expensive methods, such as DFT or other quantum mechanical methods. Instead, implicit solvation models have been developed, which have proven to yield solvation free energies close to experimentally obtained values. Implicit solvation models do not treat the solvent molecules individually and instead treat them as a dielectric continuum around the solute molecules. The continuum is shaped to fit the solute, such that it captures the solvent excluded surface (SES, see Figure 3.4) around the molecules. Typically spheres are constructed around each atom in the solute with a certain radius (e.g. van der Waals) and then the shape of the continuum is formed as the outermost overlap of the spheres to form the solvent accessible surface (SAS, see Figure 3.4). [Tomasi et al., 2005]

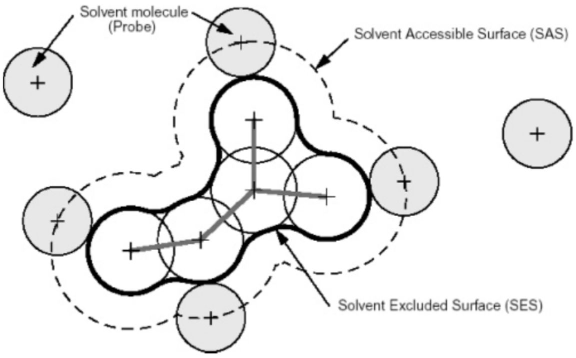

Figure 3.4. Graphic representation of the solvent excluded surface (SES) and solvent accessible surface (SAS) of a molecule using general implicit solvation approaches. The solvent molecules in the figure are probes for showing how the SES is determined. [Tomasi et al., 2005]

The cavity formed around the solute by the solvent continuum is affected by the charge distribution of the solute, which polarises the dielectric continuum. In turn, the charge distribution of the dielectric continuum polarises the solute molecule. Inside the cavity, there is a dielectric constant of 1 (corresponding to the dielectric constant of vacuum) and at the edge of the cavity, there typically is a dielectric constant of the solvent, the implicit solvation model mimics. For the Conductor-like Screening Model (COSMO), which will be used in this study, the dielectric constant of the continuum is instead set to $\epsilon = \infty$ (like a conductor) and an empirically determined scaling factor is used to obtain accurate results. While other solvent effects are in effect in real systems, handling the electrostatic effects is sufficient to replicate the solvation free energies well. [Tomasi et al., 2005; Klamt, 2018]

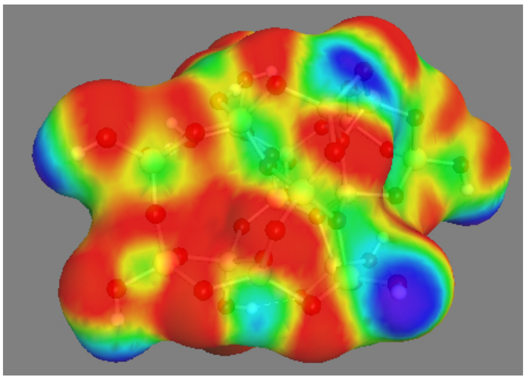

Figure 3.5. Screenshot of the cavity formed by the COSMO software in TURBOMOLE using the default settings. The molecule inside of the cavity is an aluminosilicate glass with 61 atoms.

Figure 3.5 shows the cavity created by the COSMO software in TURBOMOLE. The colours on the cavity surface reflect the local electronic distribution of the molecule.

Method 4

The procedures presented in this chapter are based on work from members of the WOODI project. The MD method is from members working at Deakin University, and the DFT method is from members working at the Technical University of Denmark. The procedures are also being used as a part of other articles which are currently in the progress of being finalised.

4.1 Molecular Dynamics

All MD simulations in this section were carried out using the LAMMPS (Large-scale Atomic/Molecular Massively Parallel Simulator) software version 3 Aug 2022 developed by Sandia National Laboratories. [Thompson et al., 2022] The simulations were run on National Computing Infrastructure (NCI) and Pawsey Supercomputer Research Centre's high-performance computing platform, Gadi. A timestep of 1 fs was used for all simulations.

4.1.1 CAS glass system

The CAS glass system was generated using the procedure in Turchi et al. [2021] where a bulk CAS glass was created with reasonable atomic-scale structural features using Guillot-Sator (GS) potential, which has been demonstrated to simulate basaltic melts well [Guillot and Sator, 2007]. The GS potential uses a Coulumbic term and the Buckingham potential for the interactions between atoms

$$E(r_{ij}) = \frac{z_i z_j}{4\pi\varepsilon_0 r_{ij}} + A_{ij} \cdot e^{-r_{ij}/B_{ij}} - \frac{C_{ij}}{r_{ij}^6}, \tag{4.1}$$

where r_{ij} is the distance between atoms i and j, z_i and z_j are the effective charges of atom i and j, respectively. A_{ij}, B_{ij}, C_{ij} are parameters for the repulsive and dispersive forces for atom pair ij. [Guillot and Sator, 2007]

First, 10,800 atoms were randomly placed in an orthorhombic simulation box with dimensions 50 Å x 50 Å x 45 Å and a composition of 43.5% CaO, 13.0 % Al_2O_3 and 43.5 % SiO_2. The composition is the same as the CAS1 glass reported in Turchi et al. [2021] which was found to be an adequate simplified model system for the stone wool glass. Comparing this composition to the molar percentages in Table 3.1, it corresponds well to the mean of the range for the typical composition of stone wool glass where all NMs are converted into CaO. This system was equilibrated at 3500 K in the NVT ensemble (constant number of atoms, volume and temperature) for 200 ps. The system was subsequently cooled to 2500 K with a cooling rate of 2.25 K/ps and then held at this temperature for 200 ps. From 2500 K, the system was cooled to 300 K with a cooling rate of 2.25 K/ps in the NPT ensemble (constant number of atoms, pressure and temperature) while applying 100 MPa pressure at 2500 K which was continuously ramped down to 0 MPa during the cooling process. Finally, the system was equilibrated at 300 K and 0 MPa pressure for 500 ps. This procedure created the amorphous bulk CAS glass system from which a slab with size 50 Å x 50 Å x 30 Å was extracted and vacuum regions with a height of 25 Å in the z-direction were introduced above and below this cut sample, thus creating a periodic slab of CAS. Three slabs were extracted from the same bulk glass CAS system at different positions yielding unique CAS slabs for further processing.

4.1.2 CAS-water interface

The novel wet-GS potential was used which has recently been developed in the WOODI to be able to simulate the interface between CAS glass and bulk H_2O. [Vuković et al., 2023] (the wet-GS article is as of yet unpublished) As the name suggests, it is an extension of the GS potential by incorporating the SPC/E [Berendsen et al., 1987] H_2O model and including parameters for the O and H atoms in H_2O to interact with the atomic species in the CAS system. In order to mimic real-life CAS surfaces, a hydroxylation process of the CAS surface is performed as a part of the wet-GS potential. The wet-GS extension of the GS potential also uses the Morse and Lennard-Jones potentials for some of the added interactions in addition to the Buckingham potential in Equation (4.1). The effective charges, parameters and more details for the wet-GS can be found in Appendix A.

The hydroxylation of the CAS surface procedure occurs by opening rings in the CAS glass near the surface (within 2 Å of the top and bottom) and adding hydroxyl groups to the opened rings. The NBO near the surface (top and bottom 2 Å) are also protonated and for every 2 H added, 1 Ca atom gets removed to maintain charge balance in the glass. The wet-GS potential also uses dual Nosé-Hoover thermostats, one acting on the CAS slab and one acting on the liquid H_2O to prevent the "cold solute, hot solvent" problem. [Vuković et al., 2023]

The three CAS slabs underwent the hydroxylation procedure followed by 600 ps NPT relaxation at 300 K and 1 atm pressure. Here, the anisotropic Nosé-Hoover thermostat-barostat was used to control the temperature with a temperature damping parameter of 0.1 ps and a pressure damping factor of 1 ps. Then H_2O molecules were added to the void in the simulation box using the PACKMOL software [Martínez et al., 2009] followed by an energy minimisation. Afterwards, the CAS-water system underwent 200 ps NVT relaxation at 300 K. In the NVT ensemble, only the Nosé-Hoover thermostat was used also with a temperature damping parameter of 0.1 ps. This yielded the three CAS-water systems for analysis of the surface features.

4.1.3 Data acquisition

Before producing the trajectories for analysis, the CAS-water system underwent 50 ps of NPT relaxation at 300 K with the anisotropic thermostat-barostat settings as previously. Then the liquid H_2O was kept in the NPT ensemble and the CAS slab was changed to the NVT ensemble with a temperature damping parameter of 0.1 ps. To prevent drift of the CAS slab during the simulation, the linear momentum of the slab was adjusted to zero every 10 ps. The simulation then ran for 1 ns (1,000,000 timesteps of 1 fs) where every 1 ps (every 1,000 timesteps) the positions were recorded and saved to a trajectory file. The first 0.5 ns was used to establish a stable configuration and only the latter half of the simulation period was analysed. The trajectories were analysed using the MDanalysis tool in Python [Gowers et al., 2016].

4.1.4 Hydrogen bond analysis

The hydrogen bonding between hydroxyl groups on the NF species and H_2O molecules participating in the hydrolysis reaction has been suggested to influence the reaction by stabilising the H_2O molecules. It was, however, only determined qualitatively by inspecting the steps of the reaction pathway. [Nangia and Garrison, 2008; Kagan et al., 2014; Zhang et al., 2022] To quantitatively analyse interactions between hydroxyl groups on the surface NF species, the prerequisites for the hydrogen bonding interaction need to be defined. The literature uses different definitions for this interaction in MD simulations. The general consensus, in both computational and experimental studies, is that the distance from donor to acceptor in the hydrogen bond is somewhere between 3.0 and 3.5 Å and the angle between the vector from the acceptor and to the donor does not exceed 30° [Jedlovszky et al., 1998; Kumar et al., 2007; Wernet et al., 2005; Notman and Walsh, 2009]. For this study, the definition of a hydrogen bond is that the distance between the hydrogen bond donor and acceptor must not exceed 3.2 Å as a conservative estimate and that the angle between the vector from donor to acceptor and the bond to H of the donor must not exceed 30°. The definition is visualised in Figure 4.1.

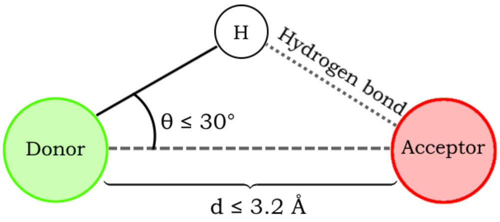

Figure 4.1. Definition of hydrogen bonds used in this study. The distance between the donor and the acceptor should not exceed 3.2 Å and the angle between the direct line between the donor and acceptor (the grey dashed line) and the donor-hydrogen bond should not exceed 30°.

This means that the distance from the surface NFs to the H_2O O atoms should at most be the length of the Si/Al to O of the hydroxyl bond + 3.2 Å in case of a completely linear hydrogen bond. The length of the bond between Si/Al and O of the hydroxyl group can be determined by a radial distribution function between the two atom groups.

4.1.5 Radial distribution function

One of the most widely used tools for computational analysis of amorphous materials is the radial distribution function (RDF). The principle of the radial distribution function is to convert the complex three-dimensional structure to a plot of essentially one-dimension where the probability of finding a certain atom type at different interatomic distances is plotted. This can be done for different pairs of atoms in the glass and the probability, *g(r)*, is calculated as

$$g(r) = \frac{\rho(r)}{\rho_0}, \tag{4.2}$$

where $\rho(r)$ is the atom density at distance r from the reference point and ρ_0 is the bulk atom density for the entire glass. This means that $g(r \to 0) = 0$ and $g(r \to \infty) = 1$ in an ideal situation. The information from an RDF is useful in identifying the bond length of different pairs of atoms in the amorphous material which can be used for structural analysis. [Du, 2019] The RDFs in this study were created using the RDF creation method in the MDAnalysis Python package [Gowers et al., 2016].

4.2 Density Functional Theory

The DFT calculations were run in the TURBOMOLE software package developed by the University of Karlsruhe [TURBOMOLE GmbH, 2021a]. The usage of the software in this study includes geometry optimisations and reaction pathway analysis using the *Woelfling* program.

4.2.1 CAS glass sphere

To construct a simplified, small-scale CAS glass system (CAS sphere) to work on, a bulk CAS system was first created using the procedure employed by another member of the WOODI project. The procedure involves creating a bulk CAS system in MD using the SHIK potential [Sundararaman et al., 2018], which was shown to yield similar bulk properties as using the GS potential [Turchi et al., 2021], and a time step of 1 fs. First, a bulk CAS glass was constructed by randomly placing 10800 atoms in a simulation box with a composition of 40 % CaO, 20 % Al_2O_3 and 40 % SiO_2. Then the system was energy minimised and afterwards heated to 3500 K and equilibrated for 500 ps in NVT ensemble. The system was cooled to 2000 K with a quench rate of 2.25 K/ps. At this temperature, a CAS sphere was extracted from the bulk which needed to match the bulk composition and lastly, the sphere was cooled to 300 K.

The next step was to transfer the CAS sphere to a simulation box of 22 Å x 22 Å x 22 Å where 300 H_2O molecules were added using the PACKMOL software. Using the reactive force field, ReaxFF[van Duin et al., 2003], and a timestep of 0.25 fs, the system was energy minimised, held in the NVT ensemble for 500 ps at 300 K and then held in the NPT ensemble for 500 ps at 300 K and 1 bar pressure. The 1 ns of simulation time allowed the system H_2O to react with the CAS sphere, resulting in hydroxyl groups forming on its surface. Finally, the hydroxylated CAS sphere was extracted from the system with H_2O and was put through semi-empirical geometry optimisation using the Mopac software[Stewart, 2013] which is a general-purpose molecular orbital package. The PM7 method was utilised and the positions of all hydrogen and oxygen atoms were fixed. The Ca atoms in the sphere caused issues for the DFT calculations and were consequently removed. This should not affect the analysis of the hydrolysis of the network forming bonds because experimentally the modifier ions are observed to leach from the system faster than the network is hydrolysed. [Okhrimenko et al., 2020; 2022] The final CAS sphere consists of 61 atoms of which 8 are Si, 8 are Al, 35 are O and 10 are H which corresponds to an aluminosilicate composition of 33.3% Al_2O_3 and 66.7% SiO_2. This means that 10 hydroxyl groups were created during the hydroxylation process. The structure of the CAS sphere for hydrolysis reaction analysis (without Ca) can be seen in Figure 4.2.

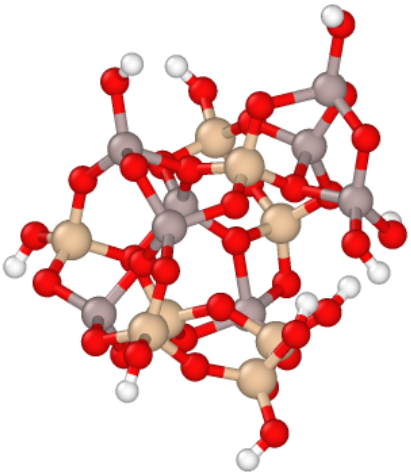

Figure 4.2. Illustration of the CAS sphere used for the DFT calculations produced using the Ovito software [Stukowski, 2010]. The initial sphere consists of 61 atoms with a charge of -4. Grey atoms are Al, brown atoms are Si, red atoms are O and white atoms are H.

4.2.2 Geometry optimisation and general considerations

For running the geometry optimisations in TURBOMOLE, the relevant H_2Os were added to the system using the Avogadro software [Hanwell et al., 2012]. The initial geometries were optimised using the Universal force field in Avogadro to obtain a reasonable starting point for geometry optimisation in TURBOMOLE. The DFT calculations used the default TURBOMOLE settings as a starting point.

The BP86 functional was employed, which integrates Becke's 1988 exchange and Perdew's 1986 correlation functionals. The BP86 is a GGA functional well-suited for most chemical systems and has a good and stable performance throughout most of the periodic system. The basis set for describing the electron wave functions was changed to TZVP (Triple-Zeta Valence Polarization), which uses a large basis set for more accurate results. The initial configuration for the molecular orbitals and occupation was provided by the extended hückel guess where the charge of the non-charge stabilised glass was entered (-4). The extended hückel guess performs an extended hückel calculation for the system to determine the orbital energy and from that determine the occupation numbers and the spatial configuration of the orbitals based on the basis set used for the calculation. In the general menu, the maximum number of iterations for the SCF (self-consistent field) calculations was set to 100, DFT was turned on, resolution of identity (RI) approximation was turned on, its memory was changed to 2500 MB and multipole accelerated RI-J (MARI-J) was turned on with the default settings. [TURBOMOLE GmbH, 2021b]. The RI approximation was used to increase the efficiency of the DFT calculation by reducing the number of repulsion integrals needed to be calculated, and MARI-J is an improvement in computational efficiency of the RI approximation without introducing significant error [Sierka et al., 2003].

4.2.3 Reaction pathway analysis

For analysis of the hydrolysis reaction, the Woelfling program from the TURBOMOLE software package was used. Woelfling determines the transition states and activation energy barriers of reactions. A description of the Woelfling program can be found in Appendix B.

The initial investigation of each reaction pathway was performed using geometry optimised structures for the reactant and product for each hydrolysis site. The first initial investigation was a Woelfling run of 100 cycles which typically did not satisfy the threshold for the gradients of the curve. The energy and reaction pathway of the 100th cycle was investigated to evaluate if it captured the hydrolysis well. If it did, the Woelfling run was continued until convergence. However, if the energy curve and the reaction pathway involved too much structural rearrangement in the system, the hydrolysis step was attempted to be isolated by manually choosing the minimum for the reaction pathway as the reactant and the first minimum after the hydrolysis step as the product. If the new reactant was not the first step of the Woelfling run, it was geometry optimised before the Woelfling run was started anew. The isolation procedure is illustrated in Figure 4.3.

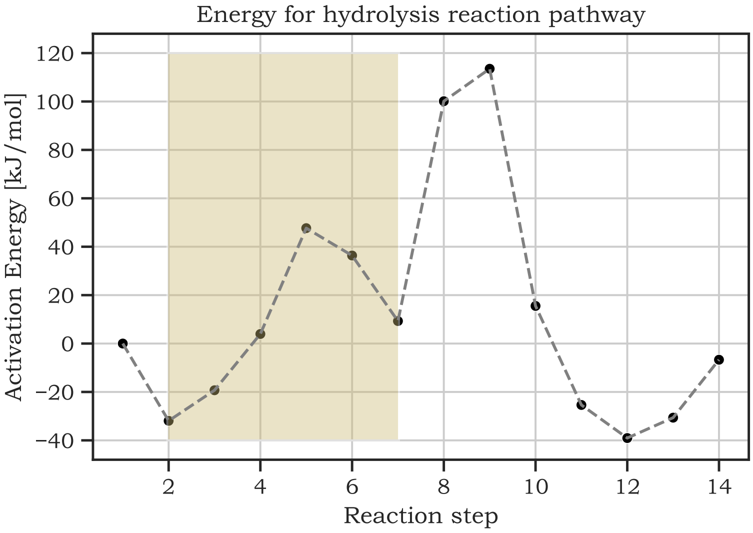

Figure 4.3. Illustration of the reaction isolation procedure for the Woelfling jobs. The yellow area is the part of the steps where the hydrolysis occurs. This energy curve is from a fully converged Woelfling job that involved a large degree of structural rearrangement which cluttered the data.

The Woelfling job in Figure 4.3 found a configuration with lower energy than the initial reactant. Therefore, the geometry at step 2 was chosen as the new starting point for the reaction. Furthermore, visual inspection of the reaction pathway determines that the highest peak directly after the coloured area stems from structural rearrangements in the system after the hydrolysis has ended. This energy is not a part of the hydrolysis reaction and therefore the step with the lowest energy after the hydrolysis has ended (step 7) was chosen as the new endpoint for the reaction.

When the Woelfling job had converged and satisfied the threshold for the energy gradients of the curve, the transition state was determined as the structure with the highest energy during the hydrolysis and the activation energy as the height hydrolysis peak relative to the starting point.

Results and discussion

5

In this chapter, the results from the MD simulations are first presented to determine relevant structural features of the CAS-water interface. Afterwards, the results from the DFT calculations for the analysis of the hydrolysis reactions are shown, followed by an overall discussion of the results. Plots in this chapter are created using Python and the matplotlib and seaborn packages.

5.1 The calcium aluminosilicate system

The CAS slabs with H_2O are prepared using the procedure presented in Section 4.1.1. The three CAS slabs with H_2O above and below are seen in Figure 5.1

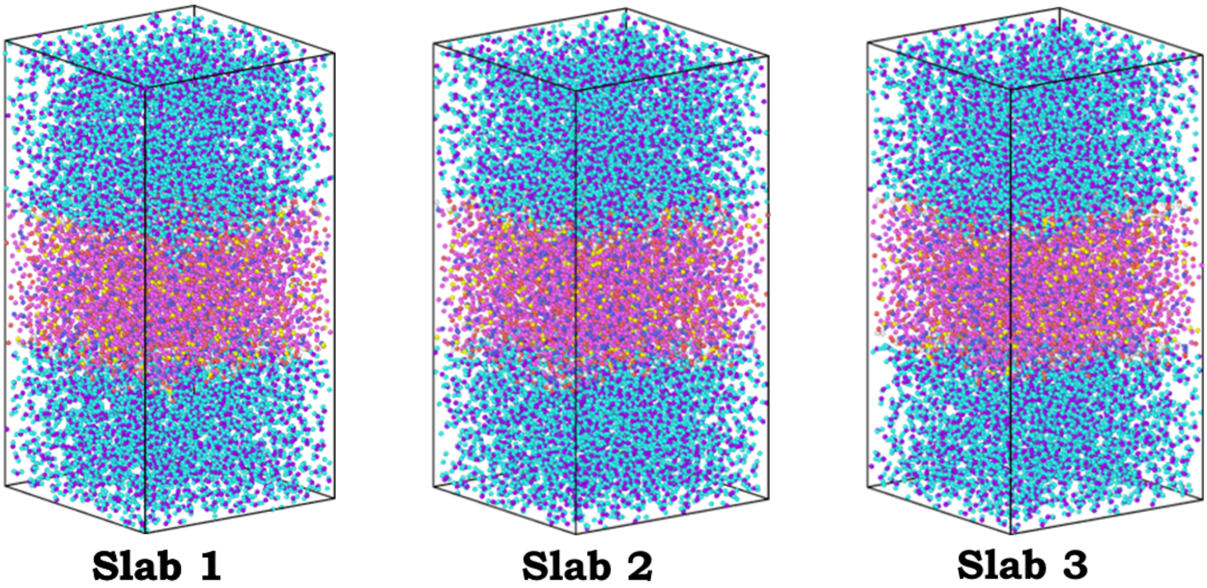

Figure 5.1. Graphical presentation of the three CAS slabs and H_2O molecules investigated in this study. The light blue atoms are H_2O H, purple atoms are H_2O O, pink atoms are O in the glass, dark red atoms are Ca, dark blue atoms are Si, yellow atoms are Al, red are hydroxyl O and white atoms are hydroxyl H. The systems are visualised using OVITO [Stukowski, 2010].

In Figure 5.1, the H_2O are the light blue and purple spheres, and the CAS slabs are placed in the middle of the simulation boxes. On the interface between the CAS glass and H_2O bulk, there are white and red spheres. These are hydroxyl groups added by the surface termination step when using the wet-GS potential to emulate real-life CAS interfaces to

H_2O. The bond lengths between O atoms and the NF and NM species in the CAS glass are determined using an RDF seen in Figure 5.2.

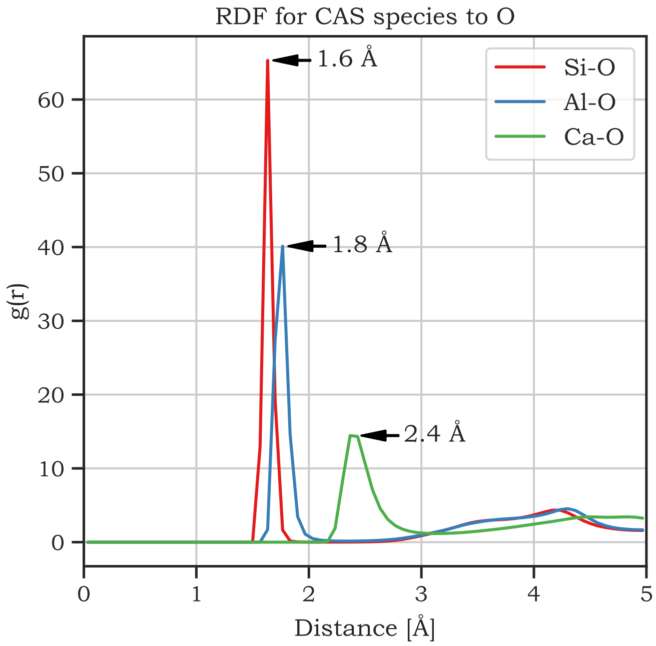

Figure 5.2. Radial distribution functions for the species in the glass, Al, Si and Ca, to the O in the amorphous system. Arrows and the associated number correspond to the x-value of the maximum for each peak.

The peaks for the RDFs of Al-O, Si-O and Ca-O are 1.6 Å, 1.8 Å and 2.4 Å, respectively. To validate the CAS glass structure in this study, the bond lengths are compared to an ab initio MD study of amorphous anorthite (25% CaO, 25 % Al_2O_3, 50 % SiO_2) [Tian et al., 2016]. The Si-O distance was found to be 1.64 Å, the Al-O distance was 1.79 Å and the Ca-O distance was 2.38 Å. The distributions also had similar shapes with sharp peaks for Si-O and Al-O and a broader distribution for Ca-O. These values are the same as those found herein. An MD study investigating the structure of different CAS compositions using the potential from [Bouhadja et al., 2014] also found similar bond lengths to those herein [Atila et al., 2019]. The length for Al-O, Si-O and Ca-O were on average 1.78 Å, 1.64 Å and 2.32 Å, respectively. The Ca-O distance is slightly lower than the value in Figure 5.2. However, the authors also observed a broader distribution for Ca-O than for the other two species. The findings from these two studies are consistent with the values in Figure 5.2, which suggests a reasonable structure of the CAS glass in this study.

5.2 Investigation of calcium aluminosilicate surface features

In this section, the results from the MD simulations will be presented. The analysis presented herein aims to gain insight into how H_2O arranges near the CAS surface.

5.2.1 Verification of the hydrogen bond definition

Before using the hydrogen bond definition presented in Section 4.1.4, it is relevant to investigate if the hydrogen bond length is observed in the distribution of separation distances between H_2O and the NF species. The bond length between the NFs near the surface and their hydroxyl groups, specifically the O in the hydroxyl groups, is useful in determining which NFs are near the surface and investigating the length of the hydrogen bonding interaction. The length of the Si/Al-OH bond is determined using an RDF which is shown in Figure 5.3.

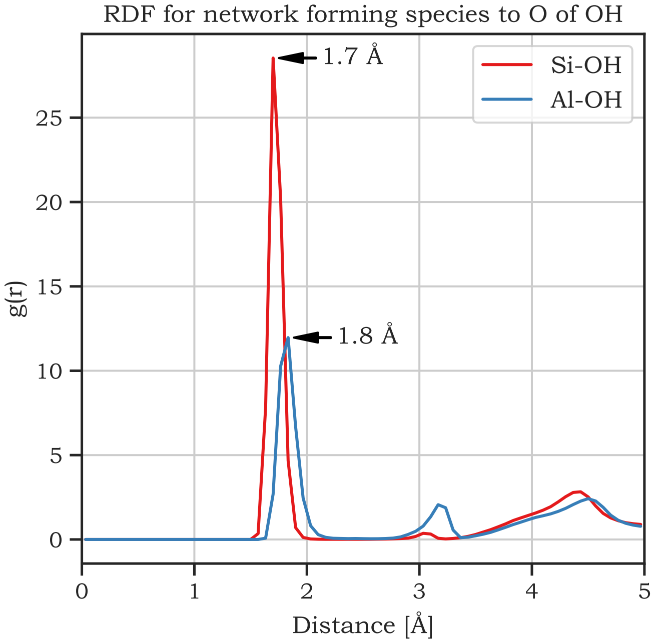

Figure 5.3. Radial distribution functions for network forming species (Al or Si) to the O of the surface hydroxyl groups. Arrows and the associated number correspond to the x-value of the maximum for each peak.

Figure 5.3 shows that the average length of the bond between the surface network forming species and the O of the hydroxyl groups are 1.7 Å and 1.8 Å for Si and Al, respectively. The Al peak has a small "shoulder", and the main peak is slightly higher than the corresponding peak in Figure 5.2. The Si to O of the hydroxyl is slightly higher than for Si to BOs in Figure 5.2. These trends are in accordance with literature where a slight increase is observed for the bond length of Si/Al to hydroxyl O compared to Si/Al to BOs. The numerical bond lengths are within 0.1 Å of their values from both first-principles calculations and MD simulations.[Kubicki et al., 1996; 2012] To capture all the surface NFs, the cut-off for the determination is set to 2.1 Å and 2.3 Å for the Si-O and Al-O, respectively. The information in Figure 5.3 is also useful in verifying the definition of hydrogen bonds introduced in Section 4.1.4. For both types of NFs, the distance between hydrogen bonded H_2O O and the surface NFs would at maximum be around 5.3 and 5.5 Å for Si and Al, respectively. RDFs for all network forming species in the CAS glass to the H_2O O atoms are presented in Figure 5.4.

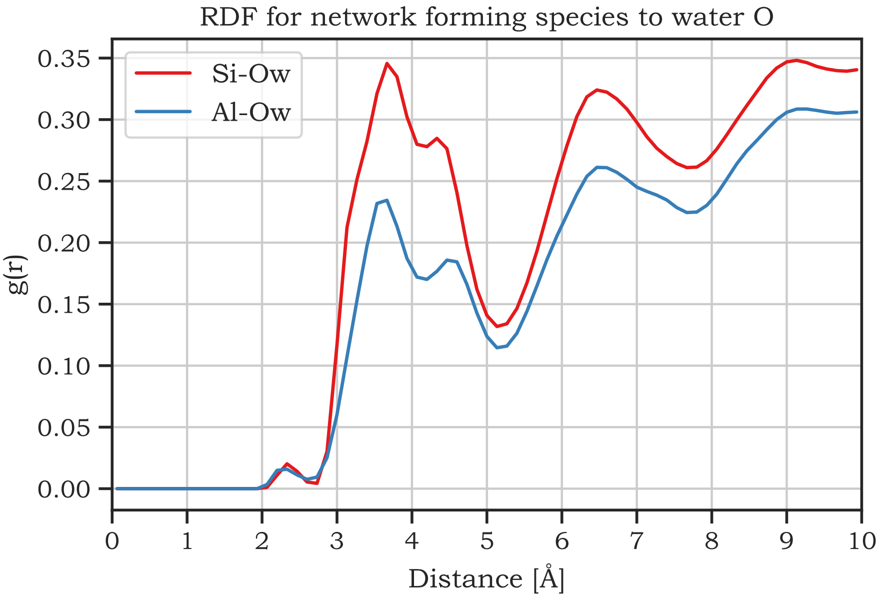

Figure 5.4. Radial distribution functions for the network forming species (Al or Si) to the H_2O O atoms.

Figure 5.4 shows RDFs for the two NF species to the H_2O O atoms (Ow). The plots show that up to a distance of about 5 Å surface interactions might occur. Beyond 5 Å, the distribution is reminiscent of bulk solvent with "layers" of H_2O near the surface ordered in steps at certain distances. It should be noted that the RDF does not approach 1 as expected for a general RDF. This is due to the nature of the system which has the bulk H_2O separated by a slab of CAS in the middle (see Figure 5.1). A closer inspection of the Si data from all three CAS slabs can be seen in Figure 5.5 with the separation distances plotted as a histogram.

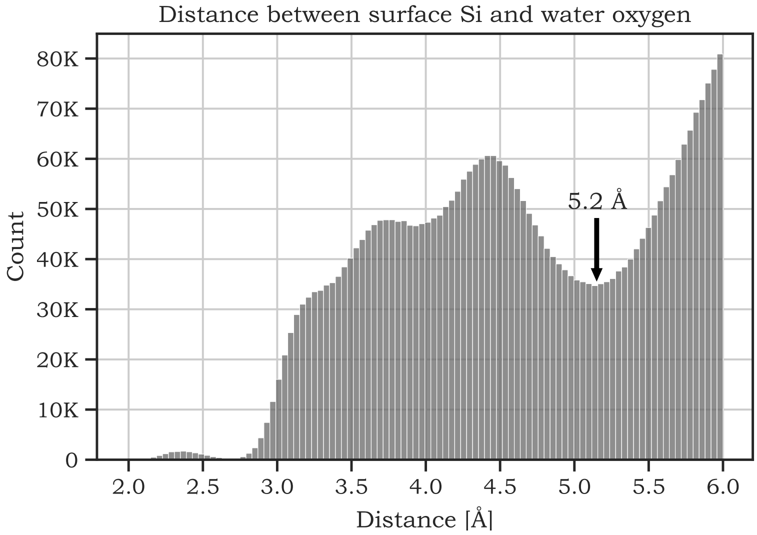

Figure 5.5. Distribution of distances between surface Si and H_2O O atoms. These data are from all three slabs. The arrow indicates the x-value of the minimum it is pointing at.

Here, a minimum at 5.2 Å corresponds well to the maximum hydrogen bond distance of 3.2 Å and a Si-OH length close to 2 Å. The small bars ranging from 2 to 2.5 Å stem from Si atoms with many hydroxyls and NBOs or Si atoms released from the surface. From 2.75 Å to 5.2 Å, Q1, Q2 and Q3 are found with no particular ordering in any of the "peaks". The relatively large distribution of distances can be attributed to the different orientations at which the hydrogen bonds can occur. A similar plot for Al is presented in Figure 5.6.

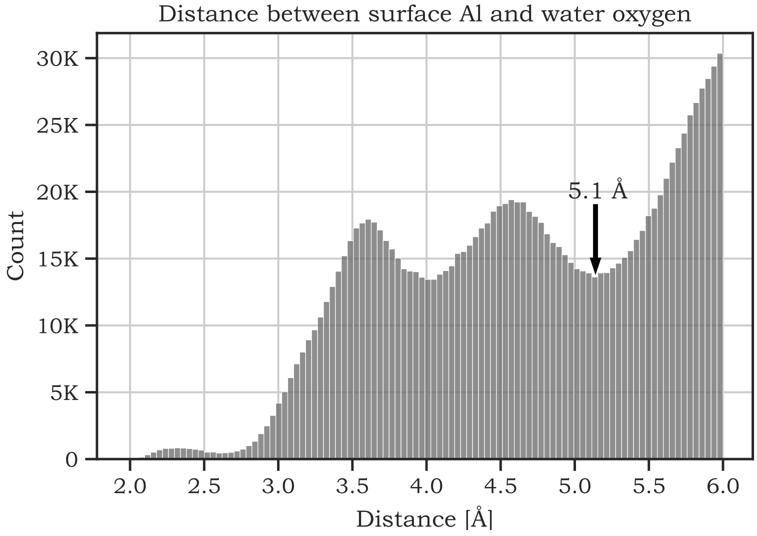

Figure 5.6. Distribution of distances between surface Al and H_2O O atoms. These data are from all three slabs. The arrow indicates the x-value of the minimum it is pointing at.

Figure 5.6 has a minimum at 5.1 Å which is slightly lower than the minimum in Figure 5.5. This is unexpected as the RDF in Figure 5.3 shows a longer length of the Al-OH bond than the Si-OH bond. It is still close to the expected minimum distance and does not reject the hydrogen bond definition from Section 4.1.4. The discrepancy can be attributed to the peak, which starts around 5 Å and rises beyond 6 Å, overlapping with the previous peak yielding a lower minimum.

The peaks for the distributions in Figures 5.5 and 5.6 <5 Å stem from different orientations for the hydrogen bond where the values closer to 5 Å have a linear configuration and values closer to 3 Å have an angled configuration with hydrogen bonding occurring parallel to the CAS slab surface. The distance of 3.2 Å for the hydrogen bond seems slightly too high. A length of 3.0 Å might be able to capture all of the hydrogen bond interactions in the system well, but to create some degree of overestimation ensures that all hydrogen bond interactions are captured.

5.2.2 Residence H_2O

The previous results are used to determine residence H_2O near the surface as these might be important for the hydrolysis of the network forming species. [Nangia and Garrison, 2008; Kagan et al., 2014; Zhang et al., 2022] Figures 5.5 and 5.6 suggests that the maximum distance for the hydrogen bonding near the surface is 5.2 Å. The distribution of the residence for H_2O O atoms that come near the surface is shown in Figure 5.7.

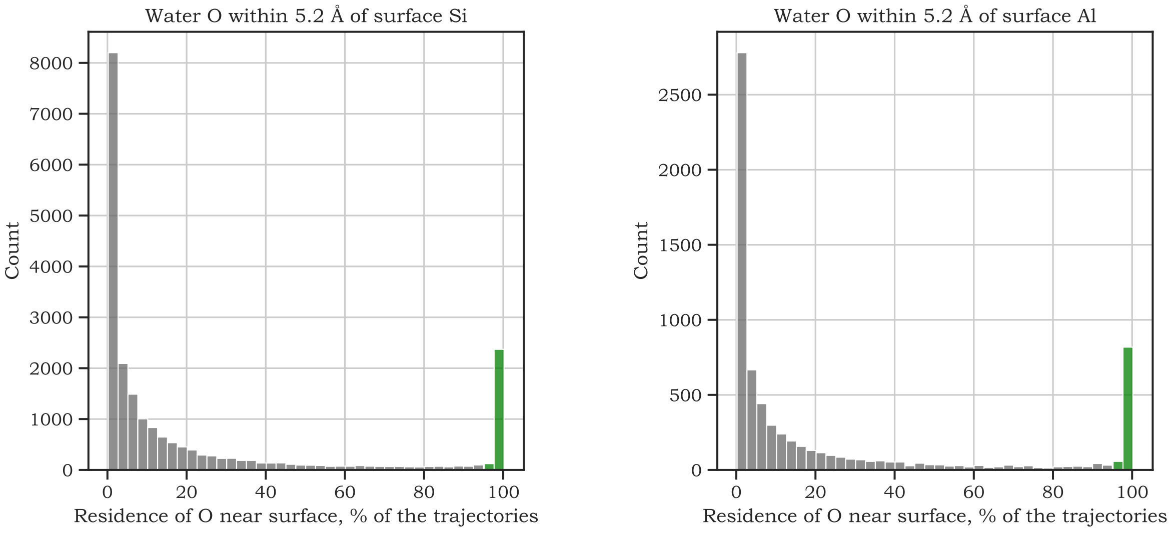

(a) (b)

Figure 5.7. Distribution of H_2O O atoms within 5.2 Å of surface NFs. (a) for Si and (b) for Al. The bars are plotted compared to how frequently they are present near the surface. 100% on the x-axis means the H_2O resides near the surface in all the analysed trajectories. The green bars represent the H_2O O atoms with a residence of more than 95%.

Figure 5.7 (a) and (b) both show that many H_2O are near the surface very briefly with a smooth decrease towards higher residence times. This is because the system contains a large amount of H_2O all rapidly switching places. However, near 100% residence, there is an increase in residing H_2O, which suggests that these are stabilised by hydrogen bonding to the OH groups on the glass surface.

5.2.3 Hydrogen bonding on the CAS-water interface

Figure 4.1 in Section 4.1.4 states that the distance between the hydrogen bond donor and acceptor must not exceed 3.2 Å and the angle between the H of the donor and the direct vector between the donor and acceptor must not exceed 30° ensuring that the hydrogen is orienting towards the acceptor. Hydrogen bonding between the CAS slab and the liquid H_2O has two cases: one where the glass is the donor and one where H_2O is the donor. In the 500 analysed trajectories, the presence of acceptable hydrogen bonding between the residence H_2O (identified in Figure 5.7) and the CAS surface where the glass acts as the donor is shown in Figure 5.8

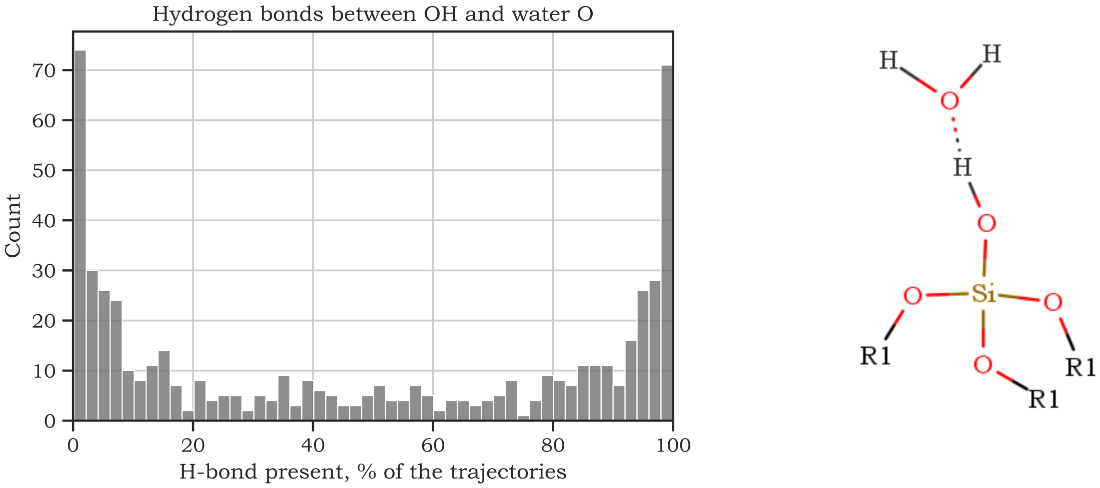

(a) (b)

Figure 5.8. (a) Distribution of hydrogen bonding presence between the surface NFs of the CAS slab to residence H_2O Os where the OH from CAS glass acts as hydrogen bond donor and the H_2O acts as the acceptor. (b) Sketch of type of hydrogen bonding investigated. The Si atom can also be an Al atom.

Figure 5.8 (a) shows a high prevalence of sites with this type of hydrogen bonding 100% of the analysed trajectories. Many also have near 100% presence, while some hydrogen bonding sites either do not exhibit this type of hydrogen bonding or only a few percent of the trajectories. The same analysis with the other type of hydrogen bonding where H_2O is the donor and the glass is the acceptor is shown in Figure 5.9.

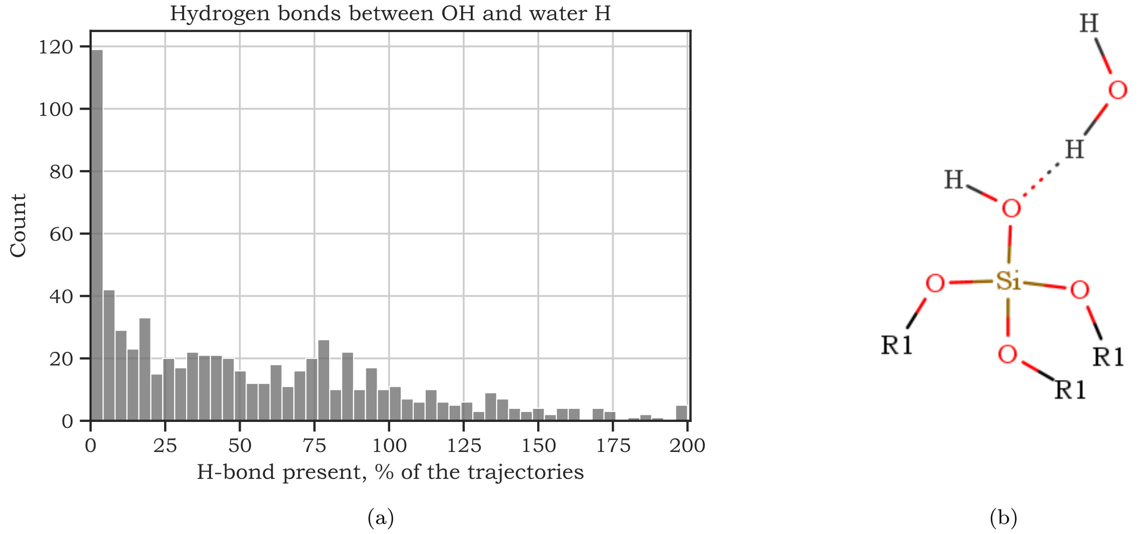

(a) (b)

Figure 5.9. (a) Distribution of hydrogen bonding presence between the surface NFs of the CAS slab to residence H_2O Os where the H_2O acts as the donor and the OH from CAS glass acts as hydrogen bond acceptor. (b) Sketch of type of hydrogen bonding investigated. The Si atom can also be an Al atom. Values exceeding 100% mean that more than one H_2O creates hydrogen bonds to the same OH group on the CAS surface.

Figure 5.9 has a more broad distribution of hydrogen bond presence than Figure 5.8 because of the possibility of making more than one hydrogen bond on each hydroxyl. This also means that the percentages on the x-axis exceed 100 % which indicates that more than one hydrogen bond is created. Comparing the higher percentages in both Figures 5.8 and 5.9, it is clear that the case where the glass acts as a hydrogen bond donor is the most prevalent of the two cases. For both plots, there is a high abundance of H_2O very briefly hydrogen bonding with the network forming species (near 0%). It is likely that most of these have hydrogen bonding of the different type and can therefore be found in the other plot. The summation of the results in Figures 5.8 and 5.9 for each hydroxyl group is shown in Figure 5.10.

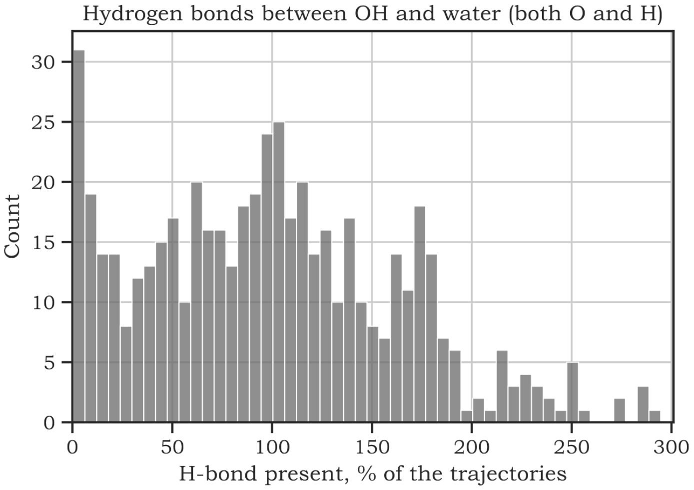

Figure 5.10. Sum of the bars in Figures 5.8 and 5.9 for each OH group. Percentages higher than 100% indicate that multiple H_2O create hydrogen bonds to the same OH group on the CAS surface.

Figure 5.10 shows that the majority of the hydroxyl groups hydrogen bond to the residence H_2O at least 100% of the trajectories. Still, some hydroxyls have less than 100% hydrogen bond presence to the residence H_2O indicating that not all of the hydroxyl groups are able to stabilise a H_2O more than 95% of the trajectories.

To simulate the complete dissolution of the NFs, i.e. stepwise hydrolysis from Q3 to Q0, it is relevant to investigate the hydrogen bonds for the differently coordinated surface NFs. This is done by grouping the plots into how many network forming bonds each NF has (Q3, Q2 or Q1). The distribution for the two types of hydrogen bonds for the three Qn groups can be found in Appendix D.1. These plots show no inclination for any of the Qn groups to deviate from the general trends found in this section; all groups show a preference to form hydrogen bonds with the glass being the donor.

This does not mean that the other type of hydrogen bonding does not occur for the two kinds of NFs. It is just not the most natural case for the H_2O to arrange in that manner. This can be ascribed to the structural degrees of freedom involved in the H_2O being the hydrogen bond donor. It needs to have a specific orientation with the H atoms of the H_2O pointing towards the O of the hydroxyl group. With the liquid H_2O being very mobile, it is difficult to maintain this position. On the other hand, the case where the CAS glass is the hydrogen bond donor is easier to maintain because the hydroxyl group is fixed on the surface of the glass and it is more lenient in terms of positions for the H_2O to be the hydrogen bond acceptor. The hydroxyl group on the surface can easily point towards the oxygen of an H_2O rather than a hydrogen of an H_2O to point at an oxygen of a hydroxyl group due to steric hindrance.

The MD analysis will be used to estimate which molecules are important for the hydrolysis. The initial objective was to find any stationary or residing solvent molecules near the surface. The analysis has shown that a large fraction of the H_2O molecules reside near the surface and are stabilised by hydrogen bonding to the hydroxyl groups on the network forming species. In the most prevalent type of hydrogen bonding, the CAS glass acts as the hydrogen bond donor and the central O in H_2O as the hydrogen bond acceptor. The opposite case does also occur but to a smaller extent.

5.3 Investigation of hydrolysis reaction pathway

DFT calculations are performed using the information obtained by the analysis of the MD data, which demonstrates evidence for H_2O stabilised by hydrogen bonding to the surface hydroxyl groups. This information will be used to place the H_2O for hydrolysis preferentially to hydrogen bond with the hydroxyl where the CAS glass acts as the hydrogen bond donor. The workflow of the reaction pathway analysis involves geometry optimisation using DFT. It is, therefore, not possible to directly include the geometry of the surface interactions from the CAS slabs from MD in the DFT calculations. Instead, the information gained from the MD simulations will be used implicitly in the initial placement of the H_2Os. The geometry optimisation scheme for the geometries keeps the hydrogen bonding placements for H_2Os to one of the hydroxyl groups. In the majority of the geometries, this is at the configuration where the glass system is the hydrogen bond donor, but in some cases, the glass is the hydrogen bond acceptor instead and this configuration is also valid. In the following section, the data for the Woelfling runs with one H_2O is presented first followed by the data for Woelfling runs with two H_2Os. Lastly, these two data sets are compared to investigate the influence of the multiple H_2Os in the calculations. Throughout this section, the linkages Si-O-Si, Si-O-Al and Al-O-Al will be referred to as Si-Si, Si-Al and Al-Al, respectively.

5.3.1 Hydrolysis with one H_2O

The activation energies for the three different types of NF linkages grouped in terms of their network coordination (Q3, Q2 and Q1) with one H_2O present in the hydrolysis are seen in Figure 5.11. The values for the plot can be found in Appendix D.2.

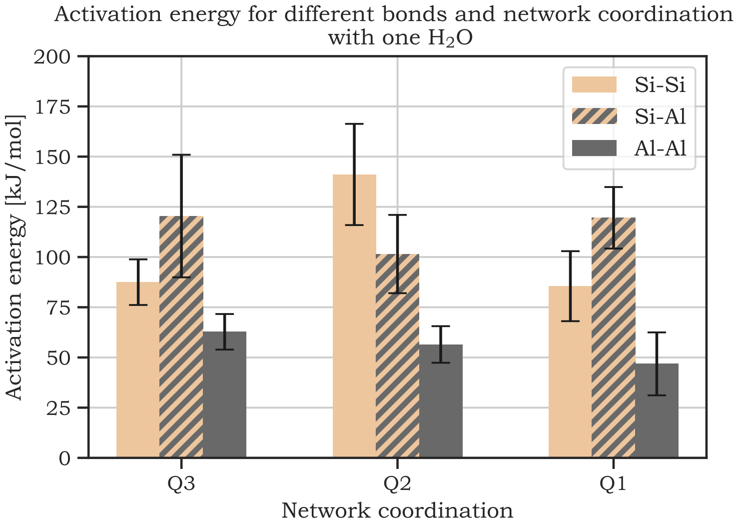

Figure 5.11. Visual presentation of the activation energies for the network linkage types (Si-Si, Si-Al and Al-Al) grouped by the number of network forming bonds (Q3, Q2 and Q1). The height of the bars are means of each group with standard deviations illustrated as the error bars.

In general, hydrolysis of the Al-Al linkage has the lowest activation energy. This has also been reported in the literature, c.f. Section 3.1.2. The hydrolysis reactions of Si-Si and Si-Al linkages seem to have similar energy barriers because their errorbars overlap for the most part, which is unexpected as the linkages involving Al were found to have lower activation energies [Morrow et al., 2009; Damodaran et al., 2022]. To compare the activation energies for the different groups, pairwise t-tests are performed with a confidence level of 95%. Due to the risk of false positives during family-wise comparisons, the significance level, $\alpha = 0.05$, is corrected using the Bonferroni correction, which yields a significance level of 0.017%. This means that the p-values presented in Table 5.1 need to be <0.017 to be significant. A Shapiro-Wilk normality test is performed to test whether the datasets can be assumed to be normally distributed as this is one of the prerequisites for performing t-tests. The statistical considerations for performing the t-tests along with the p-values from the Shapiro-Wilk normality test can be found in Appendix C.

Table 5.1. p-values for pairwise t-tests for comparing the hydrolysis of the different linkage types and groups with one H_2O. Each section of the table is mirrored on the blank diagonal. Using a confidence level of 95%, the significance level is 0.017 due to the Bonferroni correction. In cases of significant difference, the cells are coloured green.

Pair	**Q3**			**Q2**			**Q1**		
	Si-Si	**Si-Al**	**Al-Al**	**Si-Si**	**Si-Al**	**Al-Al**	**Si-Si**	**Si-Al**	**Al-Al**
Si-Si	—	0.192	0.226	—	0.065	0.007	—	0.091	0.065
Si-Al	0.192	—	0.041	0.065	—	0.002	0.091	—	0.001
Al-Al	0.226	0.041	—	0.007	0.002	—	0.065	0.001	—

Table 5.1 shows that two cases in the Q2 and one in the Q1 coordination group are significantly different while no cases in the Q3 coordination group are significantly different using the Bonferroni correction. The significant differences are found when comparing Al-Al with Si-Si and Si-Al in the Q2 group and Al-Al with Si-Al in the Q1 group. In these cases, the energy barrier for the hydrolysis of the Al-Al linkage is significantly lower than the linkages involving Si. Another interesting part about these data is that there does not seem to be a difference in energy barriers for Si-Si and Si-Al in any of the coordination groups. It has previously been reported that linkages involving Al all have lower barriers than those without, but in this case, Si increases the energy barrier more than Al decreases it. The similarity here between the Si-Si and Si-Al linkage types can be attributed to the high variance in the energies. Looking at the barplot for Q3 in Figure 5.11, the error bar of Al-Al does not overlap with the error bars of the other two groups. This indicates lower activation energy for breakage of the Al-Al linkage compared to the other two linkages. However, the differences were not found significant in Table 5.1 due to a low number of observations for the linkages in the Q3 group. It is still a strong indication of lower activation energy for breakage of the Al-Al linkage than those with Si. A similar analysis for linkage types across coordination groups can be seen in Table 5.2.

Table 5.2. p-values for pairwise t-tests for comparing the hydrolysis of the different network coordination and linkage species with one H_2O. Each section of the table is mirrored on the blank diagonal. Using a confidence level of 95%, the significance level is 0.017 due to the Bonferroni correction. No significant differences are found.

Pair	**Si-Si**			**Si-Al**			**Al-Al**		
	Q3	**Q2**	**Q1**	**Q3**	**Q2**	**Q1**	**Q3**	**Q2**	**Q1**
Q3	—	0.049	0.914	—	0.385	0.965	—	0.460	0.208
Q2	0.049	—	0.033	0.385	—	0.113	0.460	—	0.389
Q1	0.914	0.033	—	0.965	0.113	—	0.208	0.389	—

No significant differences are found for any of the coordination groups. The Q2 Si-Si linkage has the highest average energy barrier of the three Qn groups, indicating that it might be the rate limiting reaction in the complete hydrolysis of this particular linkage. On the other hand, the Q2 Si-Al linkage has the lowest average energy barrier of the three, suggesting that either Q3 or Q1 is the rate limiting reaction for this species. The Q1 Al-Al linkage has lower activation energies than Q3 and Q2. This indicates that the hydrolysis with Al-Al occurs faster with Q1 than the other two types. The activation energy is lower for Al-Al than the other two linkage types in all coordination groups, it is therefore unlikely that this linkage is present after two hydrolysis steps have already occurred. However, as no significant differences are observed, no conclusions can be made from Table 5.2.

5.3.2 Hydrolysis with two H_2Os

The activation energies for the three different types of NF linkages grouped in terms of their network coordination (Q3, Q2 and Q1) with two H_2Os present in the hydrolysis are presented in Figure 5.12. The values for the plot can be found in Appendix D.2.

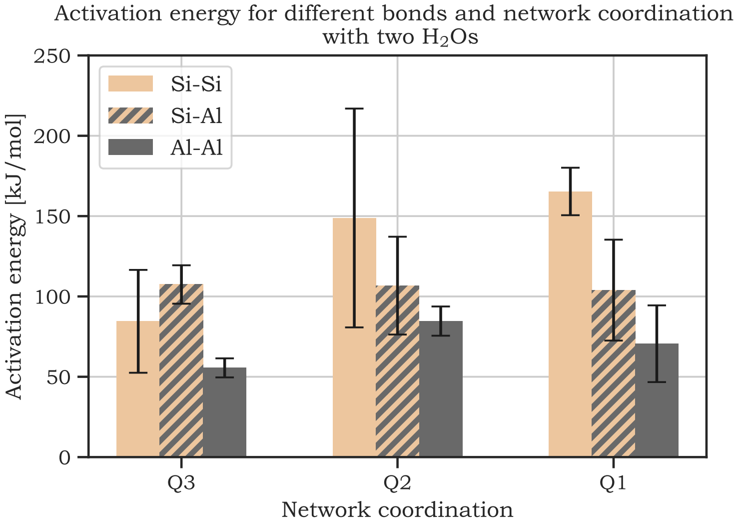

Figure 5.12. Visual presentation of the activation energies for the network linkage types (Si-Si, Si-Al and Al-Al) grouped by the number of network forming bonds (Q3, Q2 and Q1). The height of the bars are means of each group with standard deviations illustrated as the error bars.

The data shown in Table 5.3 and Figure 5.12 have a high degree of variance which is presented using the error bars in Figure 5.12. The high degree of variance stems from the structural freedom of the second H_2O which can get pushed into different energetic states during the hydrolysis reaction. The different energetic states could be either more or less energetically favourable than the initial configuration, thus creating variance in the energies of the reaction. Kagan et al. [2014] reported that the energy barriers for hydrolysis of aluminosilicate bonds are sensitive to the geometry at which the reaction occurs, i.e. how the H_2O approaches the hydrolysis site. When the second H_2O was included, the H_2O

apart of the hydrolysis reaction was placed more locally near the hydrolysis site instead of being fixed by hydrogen bonding. The geometry optimisation could therefore move the hydrolysis H_2O more around and create different initial geometries for the reaction, ultimately changing the reaction geometry.

Similar to the data for DFT calculations with one H_2O, pairwise t-tests for the dataset with two H_2Os are performed with the Bonferroni correction. The Shapiro-Wilk normality tests for these datasets are also found in Appendix C.

Table 5.3. p-values for pairwise t-tests for comparing the hydrolysis of the different species and groups with one or two molecules. Each section of the table is mirrored on the blank diagonal. Using a confidence level of 95%, the significance level is 0.017 due to the Bonferroni correction. In cases of significant difference, the cells are coloured green.

Pair	**Q3**			**Q2**			**Q1**		
	Si-Si	**Si-Al**	**Al-Al**	**Si-Si**	**Si-Al**	**Al-Al**	**Si-Si**	**Si-Al**	**Al-Al**
Si-Si	—	0.602	0.530	—	0.373	0.201	—	0.001	0.002
Si-Al	0.602	—	0.012	0.373	—	0.188	0.001	—	0.094
Al-Al	0.530	0.012	—	0.201	0.188	—	0.002	0.094	—

The p-values presented in Table 5.3 show that no difference are seen within the Q2 coordination group. For Q3, Al-Al is significantly lower than Si-Al. For Q1, Si-Si is significantly higher than the other two types. This is also apparent from Figure 5.12 where the linkage types with significant differences do not have overlapping error bars while the other ones have. A similar analysis with the three coordination groups compared within each linkage type is seen in Table 5.4.

Table 5.4. p-values for pairwise t-tests for comparing the hydrolysis of the different network coordination and linkage species with two H_2Os. Each section of the table is mirrored on the blank diagonal. Using a confidence level of 95%, the significance level is 0.017 due to the Bonferroni correction. No significant differences are found.

Pair	**Si-Si**			**Si-Al**			**Al-Al**		
	Q3	**Q2**	**Q1**	**Q3**	**Q2**	**Q1**	**Q3**	**Q2**	**Q1**
Q3	—	0.281	0.221	—	0.966	0.795	—	0.025	0.363
Q2	0.281	—	0.707	0.966	—	0.872	0.025	—	0.405
Q1	0.221	0.707	—	0.795	0.872	—	0.363	0.405	—

Table 5.4 shows no significant differences in the activation energies for each linkage type across the coordination groups as all p-values are above the significance level. This is partly due to the high variance in the values and the relatively low number of observations in each group, which means the differences must be more pronounced to be significant.

5.3.3 Comparison of the two hydrolysis datasets

To compare the results from the two datasets, t-tests are performed again. Contrary to previous t-tests, these are not pairwise and therefore do not need to be subjected to the Bonferroni correction.

Table 5.5. T-tests of the datasets with one or two H_2Os present during the hydrolysis for each linkage type (Si-Si, Si-Al or Al-Al) in the three coordination groups (Q3, Q2 or Q1). A confidence level of 95% is used and coloured green cells indicate a significant difference between the datasets (p-value<0.05).

Group	Pair	p-value
Q3	Si-Si	0.942
	Si-Al	0.541
	Al-Al	0.399
Q2	Si-Si	0.863
	Si-Al	0.754
	Al-Al	0.023
Q1	Si-Si	0.001
	Si-Al	0.188
	Al-Al	0.207

Overall, the inclusion of the second H_2O did not significantly affect the energy barriers. Only one group, Q1 Si-Si, has a significant difference where the calculations with two H_2Os have a higher energy barrier on average than the calculations with just one H_2O. For all the other groups, the activation energies with one or two H_2Os are the same. The large error bars (large standard deviations) lead to failure to reject the null hypothesis for most of these comparisons.

The proposed geometry or orientation sensitivity also seems to have a larger effect on the Woelfling calculations with two H_2Os than it has for ones with one H_2O. For calculations with one H_2O, the H_2O is more fixed as it is hydrogen bonding with a hydroxyl group on the glass surface. On the other hand, the calculations with two H_2Os have the reaction participating H_2O locally placed at the hydrolysis site, which means that it is more prone to being put into a different arrangement during the geometry optimisation. This would result in more variance in the activation energies given that the orientation sensitivity is in effect.

The reduction of activation energies when introducing more H_2Os into the hydrolysis reaction stems from the formation of other transition states, such as proton transfer from one H_2O to another [Zhang et al., 2022]. These intermediate products were not found by the Woelfling jobs in any of the cases with two H_2Os present. The lack of reduction in activation energy when including a second H_2O can therefore be ascribed to the reaction mechanism largely remaining the same as with one H_2O. Another explanation for the lack of reduction in activation energies when introducing the second H_2O is that the

COSMO model sufficiently captures the bulk water's effect in the system. This means that introducing more H_2O would not be required to mimic the bulk solvation effect.

5.3.4 Overall discussion of hydrolysis results

One source of error present in these results is the energies associated with structural rearrangement in the system. This effect is an artefact of working with a small system due to the mobility and structural freedom of the atoms in the system. The impact of this effect is attempted to be reduced by the reaction isolation procedure described in Section 4.2 by limiting the Woelfling jobs to the specific steps where the hydrolysis occurs. In some cases, however, structural rearrangement is still occurring while the hydrolysis is undergoing. This will influence the activation barrier of the hydrolysis by either increasing or decreasing the activation energy depending on whether the system rearranges to a configuration with higher or lower energy. Reaction pathway analyses, where the reaction isolation procedure was unsuccessful in isolating hydrolysis from rearrangements, typically have abnormally high or low energy barriers. They are therefore deemed as outliers and not included in the data presented here. This effect is also difficult to completely eliminate which then becomes a source of variance in the data.

The activation energies found in this study suggest that there generally is a preference for Al-Al linkages to break first and then either Si-Si or Si-Al. The numerical values of the energy barriers are somewhat similar to what has been reported in the literature. Damodaran et al. [2022] studied MD simulation of aluminosilicate glass and performed PMF calculations. The energy barrier of Si-X (where X is either Si or Al) was found to be 129 kJ/mol, which is in the range of most observations for Si-Si and Si-Al. Some groups have lower activation barriers, but are relatively similar given their standard deviation. Additionally, the barrier of Al-X was found to be 47.3 kJ/mol which is lower than the barriers for Q3 and Q2 Al-Al and slightly higher than the Q1 Al-Al linkage barrier for the dataset with one H_2O. Taking the standard deviation for Al-Al values into account, the activation energies found in this study are relatively similar. For the dataset with two H_2O, the barrier of 47.3 kJ/mol is lower than all the Qn groups. No difference was observed for any Qn groups in their study, which is the same as herein (see Tables 5.2 and 5.4). The authors also reported differences between Si-Al and Al-Si linkages and grouped Al-Si linkages with Al-Al linkages. This has not been able to be replicated in this study (see Appendix D.3). The claim of the preferential release of Al from the system was also validated by experimental findings. Two aluminosilicate glasses with multiple NMs were exposed to distilled water at neutral pH and the concentrations in the surface layer were measured by X-ray photoelectron spectroscopy (XPS) and time-of-flight secondary ion mass-spectroscopy (TOF-SIMS). A higher decrease in the content of Al than Si in the surface layer was observed.

Kagan et al. [2014] investigated the complete hydrolysis of the Si NF in amorphous

SiO_2 starting from Q4 to Q0 using MD and the PMF method similar to Damodaran et al. [2022]. They found the average activation barrier for these hydrolysis reactions to be in the range of 45 to 59 kJ/mol, which is much lower than the values found herein. They deemed the reactions from Q3 to Q2 and from Q2 to Q1 to be rate limiting. The activation energies of the reactions have very high standard deviations, suggesting no significant differences between the Qn groups were found. The findings in Kagan et al. [2014] and Damodaran et al. [2022] of no significant difference between any Qn groups for either Si-Si or Si/Al-X confirm the conclusion herein that no difference for any Qn groups for each linkage type is found. This suggests that no particular Qn species for any of the linkage types are rate limiting in terms of energy and that the complete dissolution process is controlled by the linkage types present and their relative energy barriers. In addition, Damodaran et al. [2022] also noted that the hydrolysis barrier for the Si-Si linkage is higher in aluminosilicate than for pure silica and ascribed this to the presence of Al strengthening the network.

Zhang et al. [2022] found a Si-Si barrier of 121 kJ/mol with one H_2O and 76.1 kJ/mol with two H_2Os on systems similar to the Q1 groups presented here using DFT and no implicit solvation model. The barrier with one H_2O is higher than the value found in this study and the decrease in energy when using two H_2Os is not observed. The decrease in energy barrier when including two H_2Os in the reaction can be ascribed to the lack of a solvation model in their study. Morrow et al. [2009] reported energy barriers of 146 kJ/mol for Si-Al and 39 kJ/mol for Al-Si for Q1 species using DFT without a solvation model. Compared to the values found herein, the Si-Al barrier is relatively close to the Q1 in both datasets while considering the standard deviation of the values. Their Al-Si is similar to Q1 Al-Al, but is much lower than all Si-Al activation energies (even when separating Si-Al and Al-Si, see Appendix D.3). Again, this could be caused by the lack of solvation model in their study. Nangia and Garrison [2008] invested the Si-Si barrier using DFT with and without the *integral equation formalism for the polarizable continuum model* as the implicit solvation model. They reported values of 159 kJ/mol and 147 kJ/mol for Q1 Si-Si linkages in vacuum and using the solvation model, respectively. This shows verifies that solvation models affect the energy barriers and is important to consider when performing these types of calculations.

The lower energy barrier for the Al-Al linkages can be explained by Löwenstein's rule, which states that the aluminium tetrahedrons cannot be placed adjacent to one another. This is because Al-Al has a higher potential energy than an Al-Si linkage, meaning that the Al-Al linkage is less energetically favourable than Al-Si [Putnis, 1992]. This results in smaller activation barriers for hydrolysis of the Al-Al linkage. The higher activation energies for linkages with Si can be explained by its more favourable tetrahedral structure than Al. The higher strength of the Si-O bond than Al-O is reflected in the bond lengths in Figure 5.2, where the Si-O bond is shorter than Al-O.

An aspect that is not considered in this study is the presence of defects near the CAS surface. The presence of defects, such as rings or TBO, has been suggested to reduce the energy barrier for the hydrolysis of network forming bonds in the glass. [Walsh et al., 2000; Turchi et al., 2021] This analysis could start with MD simulations where frequent defect types near the surface could be identified. The defect types would then be replicated in DFT calculations, and the hydrolysis barrier in the presence of the specific defect types could be determined.

Conclusion 6

Using the novel wet-GS force field in Molecular Dynamics simulation, stationary (residence) H_2O molecules are found on the interface between bulk H_2O and calcium aluminosilicate (CAS) glass. The residence H_2O are observed to be stabilised by hydrogen bonding between surface hydroxyl groups on the CAS glass, introduced by a surface termination procedure when using the wet-GS force field. The most prevalent case of hydrogen bonding is where the CAS glass acts as the hydrogen bond donor.

The residence H_2Os are assumed to be a part of the hydrolysis reaction of the network forming bonds in the glass. Therefore, they are included in reaction pathway analysis using Density Functional Theory. Two reactions are investigated: one with a single H_2O molecule and one with two H_2O molecules. Three network forming linkages are present in the glass: Si-Si, Si-Al, and Al-Al. These are investigated based on the number of network forming bonds each hydroxylated surface species has (Q3, Q2 or Q1).

No significant differences are observed between the dataset with one and two H_2O molecules which is ascribed to the reaction mechanism remaining the same when introducing the additional H_2O. The Al-Al linkage has the lowest activation energy for all Qn groups. No significant differences are found between the Si-Si and Si-Al linkage. Based on the results of this study, the reaction pathway is a preferential breakage of Al-Al linkages with activation energies in the range of 47 to 85 kJ/mol. The likelihood for the Si-Si and Si-Al linkages to break is similar with activation energies in the 85 to 165 kJ/mol range. No significant differences are found across Qn groups for each network linkage. This suggests that the dissolution is controlled by the linkage types present on the surface and is not rate limited to any particular Qn group.

Perspectives

7

The chemical systems studied herein are simplified versions of the actual stone wool glass system. Many NMs were excluded in the MD simulations, and all NMs were excluded in the DFT calculations. Therefore, many aspects of the stone wool glass dissolution are not covered by the results presented in this study. Specifically, the energy of network dissolution in the presence of network modifiers has not been studied. In addition, the energy associated with the diffusion of network modifiers in the amorphous system, which will occur while the network dissolves, is not investigated. The diffusion can be studied using Free Energy Perturbation which can determine the difference in the energy of the states of the network modifier, i.e. in the amorphous system and the free, solvated state. [Grossfield et al., 2003]

Taking a step further in replicating the actual stone wool glass systems, more variables need to be considered. For the stone wool insulation products to gain mechanical strength, the wool is sprayed with a polymer binder and pressed into shape [Yue and Solvang, 2021]. This means that an organic compound covers the surface of the stone wool fibres, and the dissolution occurs on the surface of the fibres, so the presence of the organic compound will affect the dissolution. In practice, the binder does not create a homogeneous coating, but instead it arranges in discrete droplets on the surfaces [Barly et al., 2019]. This means that there are some inaccessible areas on the surface where the hydrolysis of the glass material cannot occur such that the dissolution does not occur homogeneously over the entire surface area. The binder droplets could be released from the fibre surface by dissolving the glass underneath it to make it break off and create more accessible surface area for dissolution. Ivanič et al. [2020] observed the binder polymer on the stone wool fibre surface to be degraded after installation and suggested that this occurred due to depolymerisation by hydrolysis. This would mean that the stone wool material loses hydrophobicity and its compressed structure, leading to more accessible surface area and ultimately increased dissolution of the stone wool glass. It is therefore interesting to investigate the hydrolysis of the binder resin to gain insight as to how the dissolution occurs on a more macroscopic level. The rates for hydrolysis of the binder and the glass network could be compared to determine how the binder would be released from the fibres in addition to how the presence of the organic binder affects the activation energies associated with glass dissolution.

The dissolution of stone wool systems has experimentally been demonstrated to be pH dependent, as the dissolution rate increases within acidic and basic pH ranges. [Wohlleben et al., 2017; Guldberg et al., 1998; Okhrimenko et al., 2020; 2022] Computational investigations of aluminosilicate systems also suggest pH dependence. Zhang et al. [2022] observed that charged aluminosilicate species and charged intermediates significantly affected the hydrolysis activation energies. Specifically, during the hydrolysis with two H_2Os, the addition of H^+ to the reacting H_2O (yielding OH^- and H_3O^+) reduced the activation energy significantly. The inclusion of proton donating from one H_2O to the other was also attempted during this study, but without success due to SCF errors in the DFT calculations. The variable of pH and charges on the species has not been covered, and it is therefore relevant to be included in the continued work of the WOODI project.

7.1 Alternative procedure

The initial goal for the MD simulations was to obtain a measure for where the H_2Os are placed near the surface and transfer this information to DFT calculations. However, this was unfeasible due to the many geometry optimisations required to run the reaction pathway analysis. Therefore, the focus of the MD results was changed to qualitative measurements instead. The ideal case for transferring the configurations from MD to the DFT calculations is to cut out small spheres of the CAS-water interface to be run through the reaction pathway analysis such that the structures from MD are directly used in the DFT calculations. All reaction pathway analyses would require a stable starting point, so the direct inclusion of force field-based simulation geometries into first-principles calculations appears to be an issue.

The structural rearrangement of the glass system during hydrolysis also affected the energy barriers. This was partly due to artefacts of working with such a small, unstructured system in the DFT calculations and partly due to the reaction path analysis procedure. The geometry optimisation of the product coordinates might have created an unnecessarily stable product for the hydrolysis that caused to whole geometry to shift too much to only capture the effect of the hydrolysis on the energy of the system. This can be counteracted by only breaking network forming linkages and slightly shifting the position of NFs to make room for the new hydroxyl without causing the structure to rearrange. Another way to counteract the artefact of the small system is to simply work with a bigger system. However, this limits the use of first-principle calculations, but in this case, the focus could be drawn to including a reactive element in the wet-GS force field.

Alternatively, using a force field that enables the direct inclusion of the geometry from MD into DFT without significant differences in the arrangement of the amorphous system could increase the accuracy of the calculations could also be used. A different approach is to extract small parts of the CAS-water interface using the wet-GS and insert it into a smaller system with an existing reactive force field, such as ReaxFF.

Bibliography

Atila et al., 2019. Atila, A., Ghardi, E. M., Hasnaoui, A. and Ouaskit, S. *Alumina effect on the structure and properties of calcium aluminosilicate in the percalcic region: A molecular dynamics investigation.* Journal of Non-Crystalline Solids, 525, p. 119470, 2019. doi: 10.1016/j.jnoncrysol.2019.119470.

Baral et al., 2020. Baral, K., Li, A. and Ching, W.-Y. *Ab Initio Study of Hydrolysis Effects in Single and Ion-Exchanged Alkali Aluminosilicate Glasses.* The Journal of Physical Chemistry B, 124(38), pp. 8418–8433, 2020. doi: 10.1021/acs.jpcb.0c05875.

Barly et al., 2019. Barly, S. H. Q., Okhrimenko, D. V., Solvang, M., Yue, Y. and Stipp, S. L. S. *Dissolution of Stone Wool Fibers with Phenol-urea-formaldehyde Binder in a Synthetic Lung Fluid.* Chemical Research in Toxicology, 32(12), pp. 2398–2410, 2019. doi: 10.1021/acs.chemrestox.9b00179.

Berendsen et al., 1987. Berendsen, H. J. C., Grigera, J. R. and Straatsma, T. P. *The missing term in effective pair potentials.* The Journal of Physical Chemistry, 91(24), pp. 6269–6271, 1987. doi: 10.1021/j100308a038.

Bouhadja et al., 2014. Bouhadja, M., Jakse, N. and Pasturel, A. *Striking role of non-bridging oxygen on glass transition temperature of calcium aluminosilicate glass-formers.* The Journal of Chemical Physics, 140(23), 2014. doi: 10.1063/1.4882283.

Bourhis, 2014. Bourhis, E. L. *Glass - Mechanics and Technology.* Second edition. Wiley-VCH Verlag GmbH & Co. KGaA, Weinheim, 2014. ISBN: 978-3-527-33705-7.

Campopiano et al., 2014. Campopiano, A., Cannizzaro, A., Angelosanto, F., Astolfi, M. L., Ramires, D., Olori, A., Canepari, S. and Iavicoli, S. *Dissolution of glass wool, rock wool and alkaline earth silicate wool: Morphological and chemical changes in fibers.* Regulatory Toxicology and Pharmacology, 70(1), pp. 393–406, 2014. doi: 10.1016/j.yrtph.2014.05.023.

Conrady, 2019. Conrady, R., *Thermodynamics and Kinetics of Glass.* In Musgraves, J. D., Hu, J. and Calvez, L., editors, *Springer Handbook of Glass*, 1st edition, pp. 52–60. Springer Nature Switzerland AG, Cham, Switzerland, 2019. ISBN: 978-3-319-93726-7.

Damodaran et al., 2022. Damodaran, K., Delaye, J.-M., Kalinichev, A. G. and Gin, S. *Deciphering the non-linear impact of Al on chemical durability of silicate glass.* Acta Materialia, 225, p. 117478, 2022. doi: 10.1016/j.actamat.2021.117478.

Du, 2019. Du, J., *Molecular Dynamics Simulations of Oxide Glasses.* In Musgraves, J. D., Hu, J. and Calvez, L., editors, *Springer Handbook of Glass*, 1st edition, pp. 1129–1151. Springer Nature Switzerland AG, Cham, Switzerland, 2019. ISBN: 978-3-319-93726-7.

Fletcher et al., 2017. Fletcher, R., Ling, S. and Slater, B. *Violations of Löwenstein's rule in zeolites.* Chemical Science, 8(11), pp. 7483–7491, 2017. doi: 10.1039/c7sc02531a.

Gowers et al., 2016. Gowers, R., Linke, M., Barnoud, J., Reddy, T. J. E., Melo, M. N., Seyler, S. L., Domanski, J., Dotson, D. L., Buchoux, S., Kenney, I. M. and Beckstein, O. *MDAnalysis: A Python package for the rapid analysis of molecular dynamics simulations.* Proceedings of the 15th Python in Science Conference, , pp. 98–105, 2016. doi: 10.25080/Majora-629e541a-00e.

Grossfield et al., 2003. Grossfield, A., Ren, P. and Ponder, J. W. *Ion Solvation Thermodynamics from Simulation with a Polarizable Force Field.* Journal of the American Chemical Society, 125(50), pp. 15671–15682, 2003. doi: 10.1021/ja037005r.

Guillot and Sator, 2007. Guillot, B. and Sator, N. *A computer simulation study of natural silicate melts. Part I: Low pressure properties.* Geochimica et Cosmochimica Acta, 71(5), pp. 1249–1265, 2007. doi: 10.1016/j.gca.2006.11.015.

Guldberg et al., 2000. Guldberg, M., de Mergino, A., Kamstrup, O., Furtak, H. and Rossiter, C. *The Development of Glass and Stone Wool Compositions with Increased Biosolubility.* Regulatory Toxicology and Pharmacology, 32, pp. 184–189, 2000. doi: 10.1006/rtph.2000.1418.

Guldberg et al., 1998. Guldberg, M., Christensen, V. R., Perander, M., Zoitos, B., Koenig, A. R. and Sebastian, K. *Measurement of in- vitro fibre dissolution rate at acidic pH.* The Annals of Occupational Hygiene, 42(4), pp. 233–243, 1998. doi: 10.1016/S0003-4878(98)00026-X.

Hanwell et al., 2012. Hanwell, M., Curtis, D., Lonie, D., Vandermeersch, T., Zurek, E. and Hutchison, G. *Avogadro: An Advanced Semantic Chemical Editor, Visualization, and Analysis Platform.* Journal of Cheminformatics, 4(17), 2012. doi: 10.1186/1758-2946-4-17.

IARC, 2002. IARC. *MAN-MADE VITREOUS FIBRES.* IARC MONOGRAPHS ON THE EVALUATION OF CARCINOGENIC RISKS TO HUMANS, 81, 2002.

Ivanič et al., 2020. Ivanič, A., Kravanja, G., Kidess, W., Rudolf, R. and Lubej, S. *The Influences of Moisture on the Mechanical, Morphological and Thermogravimetric Properties of Mineral Wool Made from Basalt Glass Fibers.* Materials (Basel), 13(10), p. 2392, 2020. doi: 10.3390/ma13102392.

Jedlovszky et al., 1998. Jedlovszky, P., Brodholt, J. P., Bruni, F., Ricci, M. A., Soper, A. K. and Vallauri, R. *Analysis of the hydrogen-bonded structure of water from ambient to supercritical conditions.* The Journal of Chemical Physics, 108(20), pp. 8528–8540, 1998. doi: 10.1063/1.476282.

Jones, 2015. Jones, R. O. *Density functional theory: Its origins, rise to prominence, and future.* Rev. Mod. Phys., 87, pp. 897–923, 2015. doi: 10.1103/RevModPhys.87.897.

Kagan et al., 2014. Kagan, M., Lockwood, G. and Garofalini, S. *Reactive Simulations of the Activation Barrier to Dissolution of Amorphous Silica in Water.* Physical chemistry chemical physics : PCCP, 16, pp. 9294–9301, 2014. doi: 10.1039/c4cp00030g.

Klamt, 2018. Klamt, A. *The COSMO and COSMO-RS solvation models.* WIREs Computational Molecular Science, 8(1), p. e1338, 2018. doi: 10.1002/wcms.1338.

Kubicki et al., 1996. Kubicki, J. D., Blake, G. A. and Apitz, S. E. *Ab initio calculations on aluminosilicate Q 3 species; implications for atomic structures of mineral surfaces and dissolution mechanisms of feldspars.* American Mineralogist, 81 (7-8), pp. 789–799, 1996. doi: 10.2138/am-1996-7-801.

Kubicki et al., 2012. Kubicki, J. D., Sofo, J. O., Skelton, A. A. and Bandura, A. V. *A New Hypothesis for the Dissolution Mechanism of Silicates.* The Journal of Physical Chemistry, 116(33), pp. 17479–17491, 2012. doi: 10.1021/jp300623v.

Kumar et al., 2007. Kumar, R., Schmidt, J. R. and Skinner, J. L. *Hydrogen bonding definitions and dynamics in liquid water.* The Journal of Chemical Physics, 126(20), p. 204107, 2007. doi: 10.1063/1.2742385.

Leach, 2001. Leach, A. R. *Molecular Modelling: Principles and Applications.* 2nd edition. Pearson Education Limited, Essex, England, 2001. ISBN: 0-582-38210-6.

Lee and Stebbins, 2000. Lee, S. K. and Stebbins, J. F. *The Structure of Aluminosilicate Glasses: High-Resolution 17O and 27Al MAS and 3QMAS NMR Study.* The Journal of Physical Chemistry B, 104(17), pp. 4091–4100, 2000. doi: 10.1021/jp994273w.

Martínez et al., 2009. Martínez, L., Andrade, R., Birgin, E. G. and Martínez, J. M. *PACKMOL: A package for building initial configurations for molecular dynamics* *simulations.* Journal of Computational Chemistry, 30(13), pp. 2157–2164, 2009. doi: 10.1002/jcc.21224.

Moesgaard et al., 2007. Moesgaard, M., Pedersen, H., Yue, Y. and Nielsen, E. *Crystallization in stone wool fibres.* Journal of Non-Crystalline Solids, 353(11-12), pp. 1101–1108, 2007. doi: 10.1016/j.jnoncrysol.2006.12.026.

Morrow et al., 2009. Morrow, C. P., Nangia, S. and Garrison, B. J. *Ab Initio Investigation of Dissolution Mechanisms in Aluminosilicate Minerals.* The journal of physical chemistry. A, Molecules, spectroscopy, kinetics, environment, & general theory, 113(7), pp. 1343–1352, 2009. doi: 10.1021/jp8079099.

Nangia and Garrison, 2008. Nangia, S. and Garrison, B. J. *Reaction Rates and Dissolution Mechanisms of Quartz as a Function of pH.* The Journal of Physical Chemistry A, 112(10), pp. 2027–2033, 2008. doi: 10.1021/jp076243w.

Notman and Walsh, 2009. Notman, R. and Walsh, T. R. *Molecular Dynamics Studies of the Interactions of Water and Amino Acid Analogues with Quartz Surfaces.* Langmuir, 25(3), pp. 1638–1644, 2009. doi: 10.1021/la803324x.

Okhrimenko et al., 2020. Okhrimenko, D. V., Nielsen, C. F., Lakshtanov, L. Z., Dalby, K. N., Johansson, D. B., Solvang, M., Deubener, J. and Stipp, S. L. S. *Surface Reactivity and Dissolution Properties of Alumina–Silica Glasses and Fibers.* ACS Applied Materials & Interfaces, 12(32), pp. 36740–36754, 2020. doi: 10.1021/acsami.0c09362.

Okhrimenko et al., 2022. Okhrimenko, D. V., Barly, S. H. Q., Jensen, M., Lakshtanov, L. Z., Johansson, D. B., Solvang, M., Yue, Y. Z. and Stipp, S. L. S. *Surface evolution of aluminosilicate glass fibers during dissolution: Influence of pH, solid-to-solution ratio and organic treatment.* Journal of Colloid and Interface Science, 606, pp. 1983–1997, 2022. doi: 10.1016/j.jcis.2021.09.148.

Petit et al., 1990. Petit, J.-C., Mea, G., Dran, J.-C., Magonthier, M.-C., Mando, P. and Paccagnella, A. *Hydrated-layer formation during dissolution of complex silicate glasses and minerals.* Geochimica et Cosmochimica Acta, 54(7), pp. 1941–1955, 1990. doi: 10.1016/0016-7037(90)90263-K.

Putnis, 1992. Putnis, A. *Introduction to mineral sciences.* Cambridge University Press, The Edinburgh Building, Cambridge, UK, 1992. ISBN: 978-0-521-42947-4.

Shelby, 2005. Shelby, J. E. *Introduction to Glass Science and Technology.* 2nd edition. The Royal Society of Chemistry, Cambridge, UK, 2005. ISBN: 0-85404-639-9.

Sholl and Steckel, 2009. Sholl, D. S. and Steckel, J. A. *Density Functional Theory: A Practical Introduction.* John Wiley & Sons, Ltd, Hoboken, New Jersey, 2009. ISBN: 978-0-470-37317-0.

Sierka et al., 2003. Sierka, M., Hogekamp, A. and Ahlrichs, R. *Fast evaluation of the Coulomb potential for electron densities using multipole accelerated resolution of identity approximation.* The Journal of Chemical Physics, 118(20), pp. 9136–9148, 2003. doi: 10.1063/1.1567253.

Smedskjær et al., 2010. Smedskjær, M. M., Solvang, M. and Yue, Y. *Crystallization behavior and high-temperature stability of stone wool fibres.* Journal of European Ceramic Society, 30(6), pp. 1287–1295, 2010. doi: 10.1016/j.jeurceramsoc.2009.12.009.

Stewart, 2013. Stewart, J. J. P. *Optimization of parameters for semiempirical methods VI: more modifications to the NDDO approximations and re-optimization of parameters.* Journal of Molecular Modeling, 19(1), pp. 1–32, 2013. doi: 10.1007/s00894-012-1667-x.

Stukowski, 2010. Stukowski, A. *Visualization and analysis of atomistic simulation data with OVITO-the Open Visualization Tool.* Modelling and Simulation in Materials Science and Engineering, 18(1), p. 015012, 2010. doi: 10.1088/0965-0393/18/1/015012.

Sundararaman et al., 2018. Sundararaman, S., Huang, L., Ispas, S. and Kob, W. *New optimization scheme to obtain interaction potentials for oxide glasses.* The Journal of Chemical Physics, 148(19), p. 194504, 2018. doi: 10.1063/1.5023707.

Thermal Insulation Manufacturers Association, 1993. Thermal Insulation Manufacturers Association. *Man-made Vitreous Fibers: Nomenclature, Chemical and Physical Properties.* 2nd edition. TIMA Incorporated, Washington, DC, 1993.

Thompson et al., 2022. Thompson, A. P., Aktulga, H. M., Berger, R., Bolintineanu, D. S., Brown, W. M., Crozier, P. S., in 't Veld, P. J., Kohlmeyer, A., Moore, S. G., Nguyen, T. D., Shan, R., Stevens, M. J., Tranchida, J., Trott, C. and Plimpton, S. J. *LAMMPS - a flexible simulation tool for particle-based materials modeling at the atomic, meso, and continuum scales.* Computer Physics Communications, 271, p. 108171, 2022. doi: 10.1016/j.cpc.2021.108171.

Tian et al., 2016. Tian, K., Mahmoud, M., Cozza, P., Licoccia, S., Fang, D.-C., Di Tommaso, D., Chass, G. and Greaves, G. *Periodic vs. molecular cluster approaches to resolving glass structure and properties: Anorthite a case study.* Journal of Non-Crystalline Solids, 451, pp. 138–145, 2016. doi: 10.1016/j.jnoncrysol.2016.06.027.

Tomasi et al., 2005. Tomasi, J., Mennucci, B. and Cammi, R. *Quantum Mechanical Continuum Solvation Models*. Chemical Reviews, 105(8), pp. 2999–3094, 2005. doi: 10.1021/cr9904009.

TURBOMOLE GmbH, 2021a. TURBOMOLE GmbH. *TURBOMOLE V7.5 2021*, 2021a. a development of University of Karlsruhe and Forschungszentrum Karlsruhe GmbH, 1989-2007, TURBOMOLE GmbH, since 2007; available from http://www.turbomole.com.

TURBOMOLE GmbH, 2021b. TURBOMOLE GmbH. *TURBOMOLE USER'S MANUAL, version 7.5.1*, 2021b. available from https://www.turbomole.org/turbomole/turbomole-documentation/.

Turchi et al., 2021. Turchi, M., Perera, S., Ramsheh, S., Popel, A. J., Okhrimenko, D. V., Stipp, S. L. S., Solvang, M., Andersson, M. P. and Walsh, T. R. *Predicted structures of calcium aluminosilicate glass as a model for stone wool fiber: effects of composition and interatomic potential*. Journal of Non-Crystalline Solids, 567, p. 120924, 2021. doi: 10.1016/j.jnoncrysol.2021.120924.

van Duin et al., 2003. van Duin, A. C. T., Strachan, A., Stewman, S., Zhang, Q., Xu, X. and Goddard, W. A. *ReaxFFSiO Reactive Force Field for Silicon and Silicon Oxide Systems*. The Journal of Physical Chemistry A, 107(19), pp. 3803–3811, 2003. doi: 10.1021/jp0276303.

Vrána, 2007. Vrána, T. *Impact of moisture on long term performance of insulating products based on stone wool*. KTH – The Royal Institute of Technology, School of Architecture and the built Environment, Stockholm, 2007. ISBN: 91-7178-637-1.

Vuković et al., 2023. Vuković, F., Garcia, N., Perera, S., Turchi, M., Raiteri, M. S. P. and Walsh, T. R. *Atomistic Simulations of Calcium Alumina Silicates interfaced with Water*, 2023. article in preparation to be published.

Walsh et al., 2000. Walsh, T. R., Wilson, M. and Sutton, A. P. *Hydrolysis of the amorphous silica surface. II. Calculation of activation barriers and mechanisms*. The Journal of Chemical Physics, 113(20), pp. 9191–9201, 2000. doi: 10.1063/1.1320057.

Wernet et al., 2005. Wernet, P., Testemale, D., Hazemann, J.-L., Argoud, R., Glatzel, P., M., L. G. P., Nilsson, A. and Bergmann, U. *Spectroscopic characterization of microscopic hydrogen-bonding disparities in supercritical water*. The Journal of Chemical Physics, 123(15), p. 154503, 2005. doi: 10.1063/1.2064867.

Wohlleben et al., 2017. Wohlleben, W., Waindok, H., Daumann, B., Werle, K., Drum, M. and Egenolf, H. *Composition, Respirable Fraction and Dissolution Rate of 24 Stone Wool MMVF with their Binder*. Particle and Fibre Toxicology, 14(29), pp. 1–16, 2017. doi: 10.1186/s12989-017-0210-8.

Xiao and Lasaga, 1994. Xiao, Y. and Lasaga, A. C. *Ab initio quantum mechanical studies of the kinetics and mechanisms of silicate dissolution: H+(H3O+) catalysis*. Geochimica et Cosmochimica Acta, 58(24), pp. 5379–5400, 1994. doi: 10.1016/0016-7037(94)90237-2.

Yue and Solvang, 2021. Yue, Y. and Solvang, M. *Stone and Glass Wool.* In *Encyclopedia of Glass Science, Technology, History, and Culture*, chapter 9.3, pp. 1103–1112. John Wiley & Sons, Ltd, 2021. ISBN: 9781118801017. doi: 10.1002/9781118801017.ch9.3.

Zhang et al., 2022. Zhang, C.-Y., Yu, Y.-L., Yang, H., Wang, L.-M., Zhong, M.-F., Lin, S.-M., Zhang, Z.-J., Wu, Y.-Y., Liu, Y. and Xu, W. *Description of Si and Al Release from Aluminosilicate in the Acidic Condition Using Density Functional Theory: Protonated Terminal Oxygen.* Sustainability, 14(21), 2022. doi: 10.3390/su142114390.

Parameters for the wet-GS potential

A

The functions, parameters and charges for the wet-GS potential developed by the WOODI group are found herein. The information is also found in the supplementary material of Vuković et al. [2023]. Three functions are used to describe the van der Waals interactions in the system using the wet-GS potential. These are the Morse function,

$$E(r) = A\left(e^{-2B(r-C)} - 2e^{-B(r-C)}\right), \tag{A.1}$$

the Buckingham function (X6),

$$E(r) = A\left(e^{-\frac{r}{B}}\right) - \frac{C}{r^6}, \tag{A.2}$$

and the Lennard-Jones function (LJ),

$$E(r) = 4A\left(\left(\frac{B}{r}\right)^{12} - \left(\frac{B}{r}\right)^{6}\right). \tag{A.3}$$

The Morse function is used for hydroxyl H (HH) and network former (Si and Al) interaction. The Lennard-Jones function is used for the H_2O O (OW) interactions. The Buckingham function is used for all the other interactions. The parameters for these functions are found in Table A.1. The interactions between hydroxyl O (OH) and hydroxyl H (HH) are described with a harmonic function,

$$E = k\left(r_0 - r\right) \tag{A.4}$$

where the force constant $k = 24\frac{eV}{\text{Å}^2}$ and a target bond length $r_0 = 1\text{Å}$. In addition, the harmonic function in Equation (A.4) is used for the hydroxyl O to Si or Al during relaxation when performing the surface termination procedure while overruling the other interactions for these atom pairs. Here, the parameters for hydroxyl O to Si are $k = 50\frac{eV}{\text{Å}^2}$ and $r_0 = 1.52\text{Å}$ and for hydroxyl O to Al are $k = 50\frac{eV}{\text{Å}^2}$ and $r_0 = 1.55\text{Å}$.

The charges for the wet-GS potential are found in Table A.2.

Table A.1. Parameters for the wet-GS potential. In the function column, X6 refers to the Buckingham function, and LJ refers to the Lennard-Jones function. [Vuković et al., 2023]

Interaction	**Function**	**A**	**B**	**C**
O & Ca	X6	155667.70	0.178	42.2597
O & Si	X6	50306.100	0.161	46.2978
O & Al	X6	28538.420	0.172	34.5778
O & O	X6	9022.7900	0.265	85.0921
OH & Ca	X6	155667.70	0.178	42.2597
OH & Si	X6	50306.100	0.161	46.2978
OH & Al	X6	28538.420	0.172	34.5778
OH & O	X6	9022.7900	0.3	85.0921
OH & O1	X6	9022.7900	0.3	85.0921
HH & Si	Morse	5.9	2.135	2.0
HH & Al	Morse	5.735	2.135	2.2
OW & Ca	LJ	0.06414	2.46875	-
OW & O	LJ	0.06397	3.0024	-
OW & OH	LJ	0.06397	2.8024	-
OW & OW	LJ	0.00674	3.165492	-
OW & Si	LJ	0.0001	3.6	-
OW & Al	LJ	0.0001	3.6	-

Table A.2. Charges for the different atomic species in the wet-GS potential. [Vuković et al., 2023]

Type	**q(e)**
Ca	0.945
Si	1.89
Al	1.4175
O	-0.945
OH	-0.945
HH	0.4725
OW	-0.8476
HW	0.4238

Woefling program in TURBOMOLE

B

Woelfling is included in the TURBOMOLE software package and is used to determine the transition states and activation energy barriers of reactions. The Woelfling program creates the reaction pathway with a finite number of intermediate steps using reactant and product input. Therefore, it is categorised as a chain-of-states method which is the most commonly used type of method for reaction pathway analysis. Using the geometry optimised reactant and product, 12 intermediate steps are created using a variation of the Linear Synchronous Transit method which makes linearly arranged intermediate steps between the two endpoints of the reaction pathway. The energies for these steps are calculated using the TURBOMOLE settings explained in Section 4.2.2, and the geometry is optimised each cycle until the energy curve is sufficiently smooth and goes through a first-order saddle point. This is quantified using a threshold for the root mean square of the gradient component orthogonal to the tangent on the energy curve for each step in the reaction pathway, which becomes small once the pathway passes through a first-order saddle point (at the transition state) in a continuous manner. [TURBOMOLE GmbH, 2021b]

Statistical considerations for t-tests

C

Student's t-tests are performed with the null hypothesis of no difference between the means of the populations each sample group stems from. The alternative hypothesis is that there is a non-zero difference between the sample populations. The t-tests are performed as a two-sample t-test (i.e. independent) because the samples are ideally from two different populations. Additionally, the tests are performed as two-tailed because the population means can either be greater or lower than each other, i.e. there is no prejudice of one sample being greater than the other. The prerequisite for performing t-tests are: 1. independent samples, 2. normally distributed data, and 3. similar variance between the sample populations. To test whether normal distribution of the data can be assumed Shapiro-Wilk normality test can be utilised.

In this study, the Shapiro-Wilk normality tests are performed in Python using the scipy package with default settings and a significance level $\alpha = 0.05$. Because of the size of the datasets, it can be argued whether it is reasonable to perform a normality test, as the likelihood of rejecting the null hypothesis (i.e. the dataset is not normally distributed) is very small. Groups of data with two observations are in the dataset, and the Shapiro-Wilk test cannot be performed on these, but normal distribution is instead assumed. The p-values for the Shapiro-Wilk normality tests are seen for each group of data from the dataset with one H_2O and two H_2Os are seen in Tables C.1 and C.2, respectively.

Table C.1. Shapiro-Wilk test for normality for the dataset with one H_2O present during the DFT calculations. Q3 Si-Si is N/A because only two observations are present in this group, and the normality test cannot be performed.

Pair	**Q3** p-value	**Q2** p-value	**Q1** p-value
Si-Si	N/A	0.682	0.944
Si-Al	0.782	0.441	0.113
Al-Al	0.732	0.426	0.239

Table C.2. Shapiro-Wilk test for normality for the dataset with two H_2Os present during the DFT calculations. Q3 Si-Si is N/A because only two observations are present in this group, and the normality test cannot be performed.

Pair	**Q3** p-value	**Q2** p-value	**Q1** p-value
Si-Si	N/A	0.112	0.163
Si-Al	0.284	0.420	0.641
Al-Al	0.564	0.098	0.809

Because all p-values are higher than the significance level of 0.05, the null hypothesis is not rejected in any of the cases. This means that all datasets can be assumed to be normally distributed.

Supplementary data D

D.1 Hydrogen bonding for different Qs

To investigate the hydrogen bond formation for the coordination groups, Figure 5.8 (a) and Figure 5.9 (a) are separated into how many network forming bonds each surface NF has. The plots for the Q1 group are seen in Figure D.1.

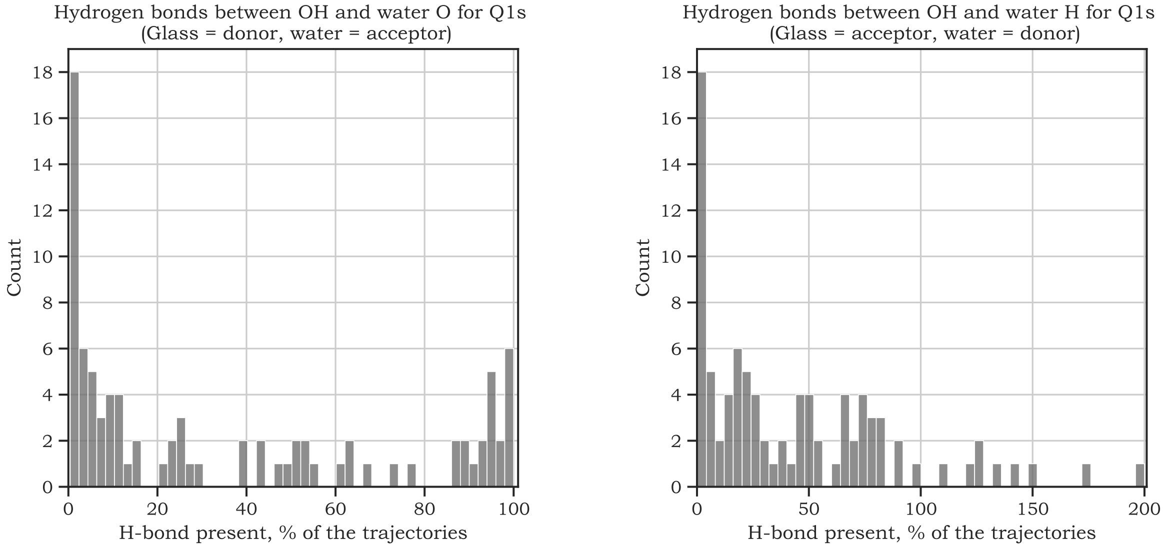

(a)

(b)

Figure D.1. a) Distribution of hydrogen bonds between the Q1 surface NFs of the CAS slab to residence H_2O O atoms where glass acts as the hydrogen bond donor. b) Distribution of hydrogen bonds between the Q1 surface NFs of the CAS slab to residence H_2O O atoms where glass acts as the hydrogen bond acceptor.

Only relatively few of the network forming species are Q1 types, causing the plots in Figure D.1 (a) and (b) to be relatively modest. Yet, the same trends as in Section 5.2.3 are still observed that the case where CAS glass as act the hydrogen bond donor (Figure D.1 (a)) is the most prevalent with more bars bar 100%. It is still less obvious because of the limited dataset for Q1 NFs. The similar plots for Q2s are presented in Figure D.2 (a) and (b).

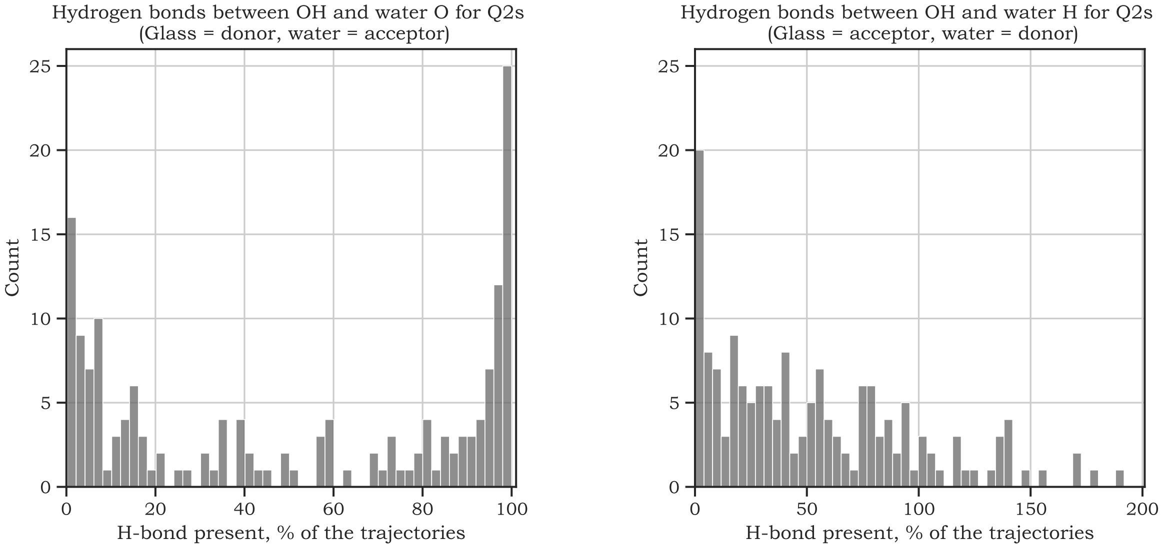

(a) (b)

Figure D.2. a) Distribution of hydrogen bonds between the Q2 surface NFs of the CAS slab to residence H_2O O atoms where glass acts as the hydrogen bond donor. b) Distribution of hydrogen bonds between the Q2 surface NFs of the CAS slab to residence H_2O O atoms where glass acts as the hydrogen bond acceptor.

It is more obvious that the case where the CAS glass is the hydrogen bond donor is the most prevalent for Q2 types of NFs. A large part of the dataset has this type of hydrogen bond present at 100% or near 100%. At the same time, relatively few observations are $\geq$ 100% for the other case (where the CAS glass is the hydrogen bond acceptor). Finally, the plots for hydrogen bonds for Q3 are shown in Figure D.3 (a) and (b).

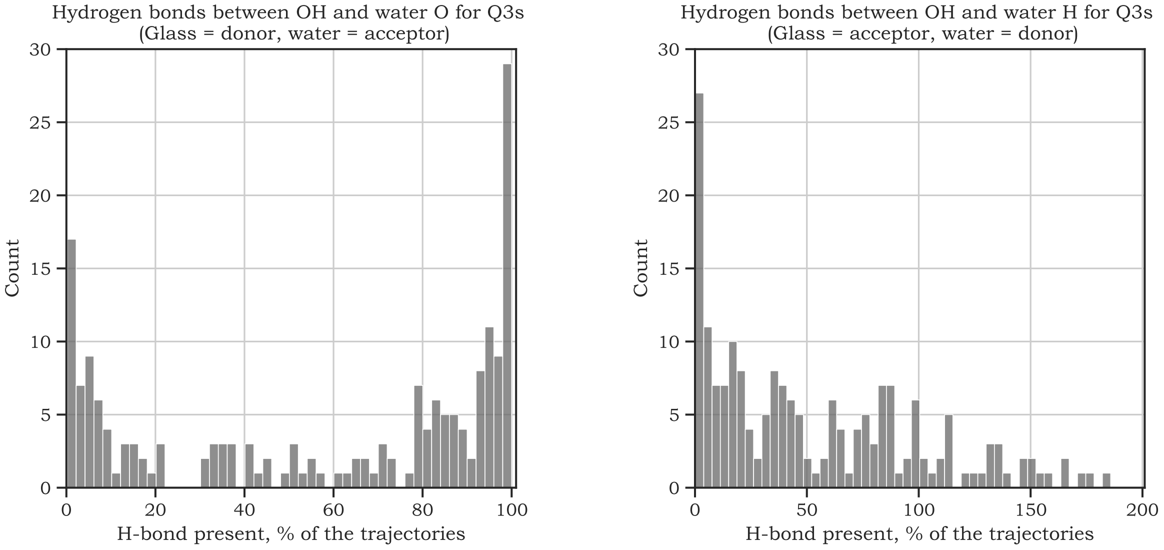

(a) (b)

Figure D.3. a) Distribution of hydrogen bonds between the Q3 surface NFs of the CAS slab to residence H_2O O atoms where glass acts as the hydrogen bond donor. b) Distribution of hydrogen bonds between the Q3 surface NFs of the CAS slab to residence H_2O O atoms where glass acts as the hydrogen bond acceptor.

Very similar plots to Figure D.2 (a) and (b) are shown in Figure D.3 (a) and (b). Again, the CAS acting as the hydrogen bond donor is the most prevalent case as it has been for the other groups of NFs. The overall conclusion from this analysis is that all Q groups exhibit a prevalence of forming hydrogen bonds with the CAS glass acting as the hydrogen bond donor.

D.2 Hydrolysis activation energies

The mean and standard deviation values for the network bond hydrolysis activation energies for each linkage type and coordination group are found herein. The values are visually presented in Figure 5.11 and Figure 5.12. The values for the dataset with one H_2O are seen in Table D.1.

Table D.1. Activation energy (Ea) for breakage of network forming bonds in the aluminosilicate glass by hydrolysis with one H_2O grouped by the linkage type (Si-Si, Si-Al and Al-Al) and the number of network forming bonds (Q3, Q2 and Q1). The Eas are the means ± standard deviation of the dataset with n observations.

Pair	**Q3**		**Q2**		**Q1**	
	Ea $[\frac{kJ}{mol}]$	n	Ea $[\frac{kJ}{mol}]$	n	Ea $[\frac{kJ}{mol}]$	n
Si-Si	87.5 ± 11	2	141 ± 25	4	85.5 ± 17	3
Si-Al	120 ± 31	4	101 ± 19	6	120 ± 15	9
Al-Al	63 ± 8.9	3	56.5 ± 9.1	5	46.8 ± 16	4

All combinations of network breakage have been investigated, which is why there are more observations for Q2 and Q1 than for Q3. In addition, some jobs were not able to converge or encountered problems with the SCF calculations and the data from these jobs are therefore missing.

The values for the dataset with two H_2Os are seen in Table D.1.

Table D.2. Activation energy (Ea) for breakage of network forming bonds in the aluminosilicate glass by hydrolysis with two H_2Os grouped by the bond type (Si-Si, Si-Al and Al-Al) and the number of network forming bonds (Q3, Q2 and Q1). The Eas are the means ± standard deviation with the dataset of n observations.

Pair	**Q3**		**Q2**		**Q1**	
	Ea $[\frac{kJ}{mol}]$	n	Ea $[\frac{kJ}{mol}]$	n	Ea $[\frac{kJ}{mol}]$	n
Si-Si	84.5 ± 32	2	149 ± 68	4	165 ± 15	4
Si-Al	107 ± 12	3	106 ± 30	6	104 ± 31	11
Al-Al	55.5 ± 5.9	3	84.7 ± 9.1	3	70.6 ± 24	4

D.3 Si-Al and Al-Si linkages

The Si-Al linkage can further be divided into Si-Al or Al-Si depending on which NF the H_2O attaches to. The activation energies for the dataset with one H_2O can be seen in Table D.3 and visually presented in Figure D.4.

Table D.3. Activation energy (Ea) for breakage of Si-Al linkage in the aluminosilicate glass separated into Si-Al and Al-Si linkages and the number of network forming bonds (Q3, Q2 and Q1) with one H_2Os present during the hydrolysis. The Eas are the means ± standard deviation with the dataset of n observations.

Pair	**Q3**		**Q2**		**Q1**	
	Ea $[\frac{kJ}{mol}]$	n	Ea $[\frac{kJ}{mol}]$	n	Ea $[\frac{kJ}{mol}]$	n
Si-Al	133 ± 25	3	104 ± 21	5	113 ± 6.1	6
Al-Si	84 ± 0	1	90 ± 0	1	132 ± 19	3

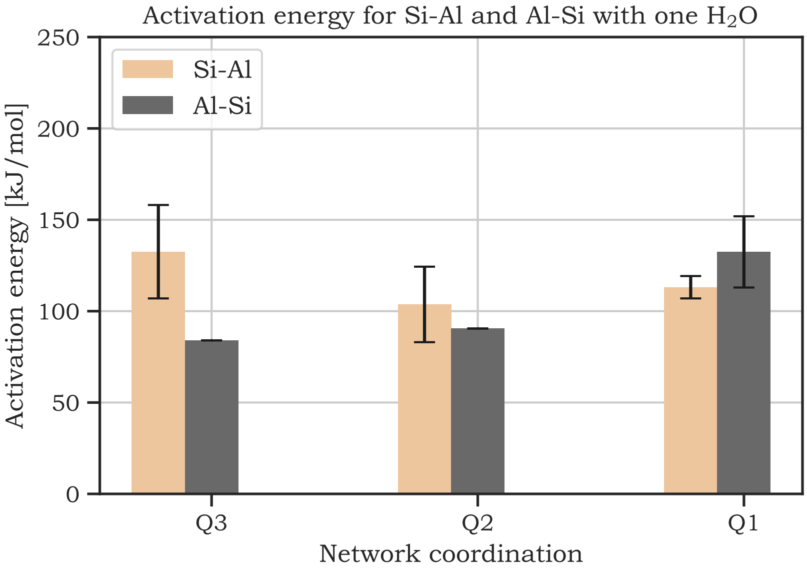

Figure D.4. Visual presentation of the means and standard deviations (illustrated with the error bars) from Table D.3.

Table D.3 and Figure D.4 show no differences in the Si-Al and Al-Si linkage for any of the groups. The error bars for Q3 Al-Si and Q2 Al-Si are absent due to only one observation in these groups. This makes it difficult to conclude anything from the Q3 and Q2 groups. The error bars for Q1 overlap indicating similar values for these groups. The same analysis is performed for the dataset with two H_2Os present during the hydrolysis. The results can be seen in Table D.4 and Figure D.5.

Table D.4. Activation energy (Ea) for breakage of Si-Al linkage in the aluminosilicate glass separated into Si-Al and Al-Si linkages and the number of network forming bonds (Q3, Q2 and Q1) with one H_2O present during the hydrolysis. The Eas are the means ± standard deviation with the dataset of n observations.

Pair	**Q3** Ea $[\frac{kJ}{mol}]$	 n	**Q2** Ea $[\frac{kJ}{mol}]$	 n	**Q1** Ea $[\frac{kJ}{mol}]$	 n
Si-Al	107 ± 12	3	109 ± 9.8	3	104 ± 32	8
Al-Si	0 ± 0	0	105 ± 42	3	102 ± 30	3

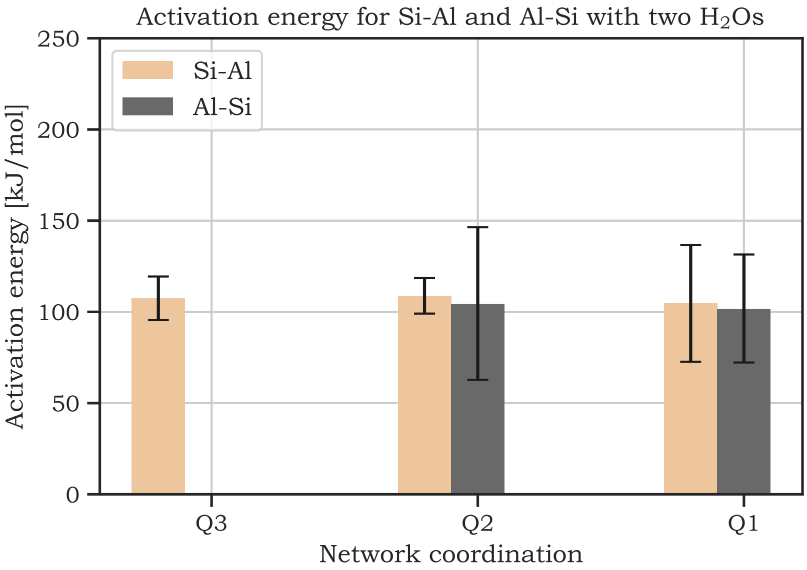

Figure D.5. Visual presentation of the means and standard deviations (illustrated with the error bars) from Table D.4.

No observations are found in the Q1 Al-Si group. Similar to the dataset with one H_2O, the error bars in Figure D.5 in the Q2 and Q1 groups overlap. All the subgroups with multiple observations have overlapping error bars in both Figure D.4 and Figure D.5. This indicates no differences between the Si-Al and Al-Si linkages. It is therefore reasonable to treat these two subgroups without distinction in the same overall group.